CELL BIOLOGY

Pellino 3 E3 ligase promotes starvation-induced autophagy to prevent hepatic steatosis

Srinivasa P. Kolapalli[1], Carsten J. Beese[1,2], Steven E. Reid[1], Sólveig H. Brynjólfsdóttir[1], Maria H. Jørgensen[1], Ashish Jain[3,4], Joyceline Cuenco[5], Monika Lewinska[2,6], Ahmad Abdul-Al[1], Aida R. López[1], Marja Jäättelä[7,8], Kei Sakamoto[5], Jesper B. Andersen[2], Kenji Maeda[7], Tor E. Rusten[3,4], Anders H. Lund[2], Lisa B. Frankel[1,2]*

Nutrient deprivation is a major trigger of autophagy, a conserved quality control and recycling process essential for cellular and tissue homeostasis. In a high-content image-based screen of the human ubiquitome, we here identify the E3 ligase Pellino 3 (PELI3) as a crucial regulator of starvation-induced autophagy. Mechanistically, PELI3 localizes to autophagic membranes, where it interacts with the ATG8 proteins through an LC3-interacting region (LIR). This facilitates PELI3-mediated ubiquitination of ULK1, driving ULK1's subsequent proteasomal degradation. PELI3 depletion leads to an aberrant accumulation and mislocalization of ULK1 and disrupts the early steps of autophagosome formation. Genetic deletion of Peli3 in mice impairs fasting-induced autophagy in the liver and enhances starvation-induced hepatic steatosis by reducing autophagy-mediated clearance of lipid droplets. Notably, PELI3 expression is decreased in the livers of patients with metabolic dysfunction–associated steatotic liver disease (MASLD), suggesting its role in hepatic steatosis development in humans. The findings suggest that PELI3-mediated control of autophagy plays a protective role in liver health.

INTRODUCTION

During evolution, cells have developed mechanisms to monitor and respond to fluctuations in nutrient abundance. Conditions of nutrient scarcity demand for a tightly coordinated adaptive response to safeguard cellular integrity (*1*, *2*). Macroautophagy (hereafter referred to as autophagy) is highly up-regulated in response to starvation, where it plays a crucial role in maintaining cellular and tissue homeostasis through the delivery of cytoplasmic components for lysosomal degradation and recycling (*3*). During autophagy initiation, double-membrane structures form in close contact with the endoplasmic reticulum, giving rise to the early autophagosomal membrane, also known as the phagophore (*4*, *5*). Phagophores expand through a highly controlled process to form mature autophagosomes that fuse with lysosomes to degrade the engulfed cargo. In response to starvation in animals, autophagy is a critical mechanism for internal energy generation and vital for survival (*3*). Tissues with high metabolic activity, including muscle, brain, and liver, are particularly vulnerable to autophagy dysfunction (*6*). During conditions of nutrient scarcity, the liver is a major site of excess lipid accumulation within lipid droplets (LDs) (*7*). Here, autophagy-mediated degradation of LDs plays a crucial role in the catabolism and mobilization of intracellular lipids to meet energy requirements (*7*, *8*). Autophagy has therefore been attributed an important role in protection against hepatic steatosis, with relevance in liver pathologies such as metabolic dysfunction–associated steatotic liver disease (MASLD), where aberrant lipid accumulation represents a central pathological hallmark (*9*).

A master coordinator of the early steps of phagophore formation is the unc-51–like autophagy-activating kinase 1 (ULK1) complex, comprising ULK1 and its adaptor proteins autophagy-related protein 13 (ATG13), ATG101, and focal adhesion kinase (FAK)–interacting protein of 200 kDa (FIP200) (*10*–*12*). ULK1 senses and integrates upstream signals of nutrient and energy availability and initiates autophagy through recruitment of the vacuolar protein sorting 34 (VPS34) complex to the phagophore (*13*). The subsequent generation of phosphatidylinositol 3-phosphate (PI3P) serves as a platform for the further recruitment of PI3P-binding proteins, such as WD repeat domain phosphoinositide-interacting protein 2 (WIPI2B) and double FYVE containing protein 1 (DFCP1), essential for membrane nucleation and expansion (*14*, *15*). During phagophore expansion, the LC3 and GABARAP subfamily members (orthologs of the yeast ATG8 protein) are conjugated to the inner and outer surface of the phagophore by lipidation. These proteins participate in crucial steps of phagophore expansion, cargo recruitment, and autophagosome closure (*16*, *17*).

Upon autophagy induction, the steady-state levels of core autophagy machinery proteins are fine-tuned through the coordinated balance of protein production and degradation, serving to restrain or potentiate a highly adaptable response to fluctuating demands. Contributing to this, autophagy proteins undergo turnover through degradation pathways such as autophagy itself or the proteasome, most often controlled by posttranslational modifications such as ubiquitin (*18*–*20*). For instance, oscillations of ULK1 protein levels during the starvation response are regulated by a tight interplay between its degradation and renewed production. Contributing to this are E3 ligases such as neural precursor cell expressed developmentally down-regulated gene 4-like (NEDD4L) and cullin 3 (CUL3)–kelch-like protein 20 (KLHL20), which ubiquitinate ULK1 to mediate its timely degradation by the proteasome (*21*, *22*). Likewise, WIPI2 is directed for proteasomal degradation by the E3 ligase HECT, UBA,

[1]Cellular Homeostasis and Recycling, Danish Cancer Institute, DK-2100 Copenhagen, Denmark. [2]Biotech Research and Innovation Centre, Faculty of Health and Medical Sciences, University of Copenhagen, DK-2200 Copenhagen, Denmark. [3]Center for Cancer Cell Reprogramming, Faculty of Medicine, University of Oslo, Oslo, Norway. [4]Department of Molecular Cell Biology, Institute for Cancer Research, Oslo University Hospital, Oslo, Norway. [5]Novo Nordisk Foundation Center for Basic Metabolic Research, University of Copenhagen, DK-2200 Copenhagen, Denmark. [6]Gubra, DK-2970 Hørsholm, Denmark. [7]Cell Death and Metabolism, Center for Autophagy, Recycling and Disease, Danish Cancer Institute, DK-2100 Copenhagen, Denmark. [8]Department of Cellular and Molecular Medicine, Faculty of Health Sciences, University of Copenhagen, DK-2200 Copenhagen, Denmark.
*Corresponding author. Email: frankel@cancer.dk

and WWE domain containing E3 ubiquitin protein ligase 1 (HUWE1) (*23*), and ATG16L1, a key player in phagophore expansion and LC3/GABARAP lipidation, is ubiquitinated and targeted for autophagic and proteasomal degradation by the E3 ligase Gigaxonin (*24*). Interference with the timely degradation of these key factors can lead to their mislocalization and/or to the accumulation of dysfunctional autophagy machinery, causing impairment of autophagosome formation (*24*). Degradation of autophagy machinery further participates in a positive feedback regulation to permit the rapid onset of new rounds of autophagosome formation (*19*).

To elucidate players in the ubiquitin-mediated regulation of autophagy, we performed a high-content live-cell image-based screen of the human ubiquitome. Among the top candidates, we identify Pellino 3 (PELI3) as a crucial regulator of starvation-induced autophagy. PELI3 is an E3 ligase, previously implicated in inflammatory signaling pathways including Toll-like receptor signaling, tumor necrosis factor (TNF), and nucleotide binding oligomerization domain containing 2 (NOD2) pathways (*25*–*27*), while its role in autophagy regulation remains uncharacterized. We describe how PELI3 is recruited to autophagic membranes where it interacts directly with ATG8 proteins through an LC3-interacting region (LIR). By controlling ULK1 steady-state levels during nutrient deprivation, we find that PELI3 is required for the early steps of autophagy. We further report that ablation of Peli3 leads to defective autophagy in the liver of mice challenged by nutrient deprivation, resulting in the accumulation of autophagy substrates including p62 aggregates and ubiquitinated proteins. Moreover, we find that deletion of Peli3 exacerbates starvation-induced hepatic steatosis by reducing autophagy-mediated clearance of LDs. We identify a reduced expression of Peli3 in livers from patients with MASLD, suggesting its potential implication in the development of hepatic steatosis in humans.

RESULTS

A high-content image-based ubiquitome screen identifies regulators of starvation-induced autophagy

To identify regulators of starvation-induced autophagy, we performed a high-content image-based screen in which we targeted a total of 1192 ubiquitin-modifying proteins, including ubiquitin interactors, E1, E2, and E3 ligases, as well as deubiquitinases (Fig. 1A and table S1). Each gene was targeted with three independent small interfering RNAs (siRNAs) during bulk autophagy induction by long-term starvation without amino acids and with reduced levels of glucose [24 hours in Hanks' balanced salt solution (HBSS)]. We monitored the autophagic degradation of ribosomes, which are known to comprise a major cargo substrate for bulk autophagy during a prolonged starvation response (*28*). We utilized human Tig3 fibroblasts expressing doxycycline-inducible ribosomal protein 10A (RPL10A) coupled to the pH-sensitive mKeima fluorophore that emits red fluorescence in an acidic environment (*29*). As a readout, we monitored RPL10A recruitment to acidified lysosomes by automated quantification of red mKeima puncta by live-cell microscopy (Fig. 1A). Confirming the specificity of this readout, we observed a clear colocalization of mKeima puncta with lysosomes (fig. S1A). The use of an inducible mKeima-RPL10A expression, which was turned off during the 24-hour autophagy induction, allowed us to exclusively monitor the degradation of a preexisting pool of mature ribosomes as a bulk autophagic cargo (Fig. 1A). For further details on the screen setup, see Materials and Methods.

Two independent repetitions of the primary screen showed high reproducibility (fig. S1B), and the positive screen controls spotted on each plate (siBECN1 and siULK1) showed a robust effect window relative to the negative siControl (Fig. 1A and fig. S1C). For candidate selection, we performed a redundant siRNA activity (RSA) analysis to rank the siRNAs by effect potency and additionally prioritize candidates with multiple scoring siRNAs (*30*). By setting significance thresholds of $P < 0.05$ and at least two siRNAs scoring outside the RSA boundaries (fig. S1C), we identified 79 candidates. Among these, the knockdown of 60 caused a reduction in lysosomal mKeima puncta, while the knockdown of the remaining 19 resulted in an up-regulation of puncta (Fig. 1B). Among 79 candidates, 5 were excluded due to extensive cell death and the remaining 74 were subjected to a validation screen using the two best of three original siRNAs per gene. In addition to the original Tig3 mKeima-RPL10A cells, the validation screen was also performed in Tig3 mKeima-LC3B–expressing cells to assess an independent reporter of bulk autophagic flux (Fig. 1A). This screen validated 57 of 74 candidates for the Keima-RPL10A cell line, while 35 were validated in the Keima-LC3B cells, suggesting that these candidates robustly affect bulk autophagy flux without selectivity for ribosomes (Fig. 1C). Qualifying the screen, several known autophagy regulators were found among the top candidates including VPS11, OTU domain-containing protein 7B (OTUD7B), RING finger protein 31 (RNF31), and ubiquitin-specific peptidase 10 (USP10) (*31*–*34*). We narrowed our focus to candidates for which depletion resulted in a reduction of mKeima puncta by at least 50% in both reporter cell lines relative to siControl [fold change (FC) < 0.5], leading to a selection of 19 lead candidates (Fig. 1, C and D).

The E3 ligase Peli3 promotes starvation-induced autophagy

Among the top 19 candidates identified from the validation screen (Fig. 1D), the candidate with both the strongest and most consistent effect between independent siRNAs was the E3 ubiquitin ligase PELI3. Intrigued by the limited information on this protein, mainly characterized in the context of innate immune signaling, we decided to explore its role in autophagy regulation. Representative images from the validation screen demonstrate the reduction in mKeima-LC3B and mKeima-RPL10A puncta after PELI3 depletion in Tig3 cells (fig. S1, D and E). This was further confirmed by a reduction in lysosomal processing of mKeima, as evidenced by a decrease in the 25-kDa cleavage product in both cell lines after PELI3 depletion (fig. S1, F and G). Verifying the block in autophagic flux, we observed an accumulation of the p62 cargo protein and a reduction in LC3B lipidation after PELI3 knockdown (fig. S1H). As in the screen, depletion of ULK1 was included as a positive control in these validations, resulting in comparable effects (fig. S1, F to H). Knockdown efficiencies of >90% for each PELI3 siRNA were confirmed by reverse transcription quantitative polymerase chain reaction (RT-qPCR) (fig. S1I).

Because the screen and associated validations were performed after long-term starvation (originally chosen due to a robust effect window for ribosomal cargo), we investigated whether PELI3 also had an impact on early autophagy signaling events after 2-hour starvation. Using immunofluorescence microscopy, we observed a significant decrease in the number of starvation-induced LC3B and ATG16L1 puncta in Tig3 cells after Peli3 depletion (Fig. 1, E and F). Likewise, using transmission electron microscopy (TEM), we observed that PELI3-depleted cells contained significantly fewer autophagic vesicles

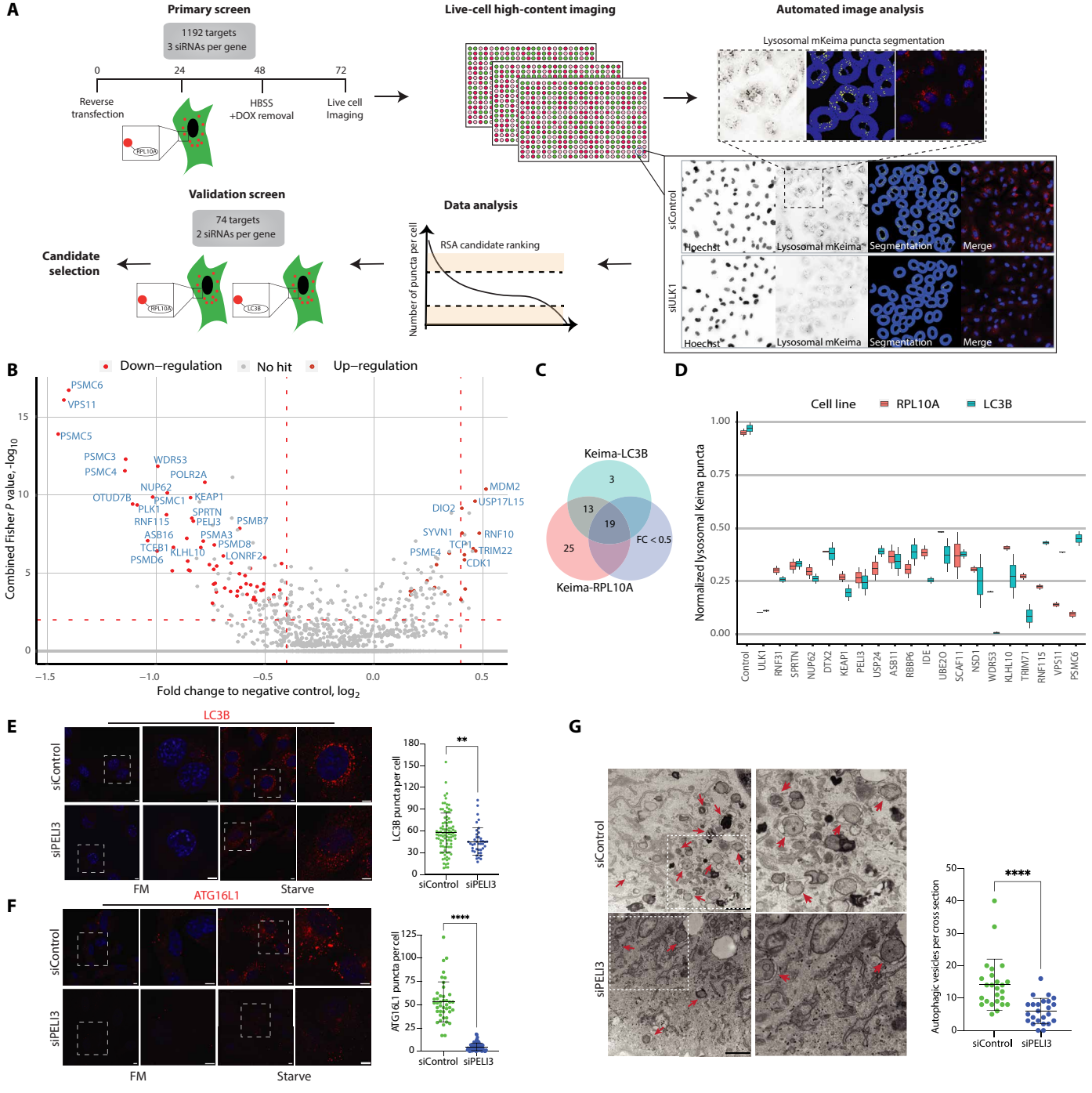

Fig. 1. High-content screen identifies PELI3 as a regulator of starvation-induced autophagy. (**A**) Schematic of primary and validation screens. Readout is based on quantification of red mKeima puncta per cell. Representative images of siControl and siULK1 demonstrate image segmentation and feature collection of perinuclear mKeima puncta from acid pH (excitation ~586 nm). (**B**) Screening results plotted as $\log_2$ of the mean FC of the three siRNAs for each gene relative to the negative control against the $-\log_{10}$ of the combined *P* value. Selected candidates (RSA analysis) are annotated in red. (**C**) Venn diagram depicts overlap of significant hits from both cell lines of the validation screen with the FC criteria <0.5. (**D**) Lysosomal mKeima puncta for 19 candidates fulfilling the selection criteria from (C). Data are depicted as the mean of two siRNAs from two independent repetitions. Data normalized to positive (ULK1) and negative (Control) control siRNAs. (**E** and **F**) Representative images (60×) of Tig3 cells (72-hour transfection) in full medium (FM) or starved in HBSS for 2 hours, immunostained for LC3B (E) or ATG16L1 (F). Nuclear stain with Hoechst 33342. Magnified inserts of highlighted areas on the right. Scale bar, 5 μm. The number of puncta was quantified from ≥100 cells, and the data represent mean ± SD number of puncta per cell. ATG16L1 ($n = 2$) and LC3B ($n = 3$). ****$P < 0.0001$. (**G**) TEM analysis of Tig3 cells (72-hour transfection) starved for 2 hours (HBSS) in the presence of 200 nM BafA1 before fixation. Representative images are shown. Scale bar, 1 μm. Images displayed on the right are cropped and magnified from the highlighted area. Red arrows denote autophagic vesicles. Quantification of mean number of autophagic vesicles ± SD per cross section ($n \geq 25$ cross sections). Statistical analysis [(E) to (G)] was performed by unpaired Student's *t* test. **$P < 0.01$, ****$P < 0.0001$.

(Fig. 1G). These data suggest a more immediate role for PELI3 at the early steps of autophagosome formation, also during short-term starvation.

Reduced autophagy in the liver of Peli3-deficient mice results in the accumulation of autophagic substrates

Having established a role for PELI3 in the regulation of autophagy at the cellular level, we proceeded to investigate the effects of Peli3 on autophagy in mice. We generated whole-body Peli3 knockout (KO) mice where the critical exon 3, which is present in all isoforms, was removed (see Materials and Methods for details) (fig. S2A). We confirmed the mouse genotypes by PCR-based detection of wild-type (WT) or mutant alleles (fig. S2B), and we further confirmed a lack of Peli3 mRNA expression by RT-qPCR in Peli3 KO mouse livers (fig. S2C). Mouse embryonic fibroblasts (MEFs) from day 13.5 Peli3 KO or WT embryos were subjected to 2-hour starvation in the presence or absence of the lysosomal acidification inhibitor bafilomycin A1 (BafA1). Assessment of lipidated LC3B and p62 levels suggested a reduction of starvation-induced autophagic flux in Peli3-deficient MEFs, most prominent after BafA1 treatment (fig. S2D). In addition to starvation as a stimulus for autophagy, a similar reduction in LC3B lipidation was observed after treatment with the mTOR inhibitor PP242 (fig. S2E).

Peli3 KO mice fed on a standard chow diet develop normally, are fertile, and do not display any overt phenotypes (https://www.mousephenotype.org/data/genes/MGI:1924963). To assess the effects of Peli3 in the context of the starvation response, we subjected 6-week-old mice to an overnight starvation period (16 hours) followed by analysis of tissue from a selection of organs known to have a high dependency on autophagy including liver, brain, muscle, heart, and lung (Fig. 2, A to D, and fig. S2F). We investigated total levels of autophagic cargos p62 and ubiquitinated proteins, commonly used to report on changes in autophagy in tissue (*35*, *36*). While there were no clear trends in the muscle, brain, heart, or lung tissues (fig. S2F), the livers of Peli3-deficient mice displayed consistently enhanced levels of p62 and ubiquitin (Fig. 2, B and C), suggestive of a defect in autophagic flux resulting in cargo accumulation. We focused on the liver due to previous implications for Peli3 in liver pathologies (*37*, *38*) as well as the major importance of hepatic autophagy during acute starvation for maintenance of liver homeostasis (*39*, *40*). Through immunohistochemical analysis of cross-sectioned livers from starved mice, we confirmed increased levels of both p62 and ubiquitin in Peli3 KO relative to WT mice (Fig. 2D). The accumulation of these cargos coincided with reduced levels of lipidated LC3B as well its family member GABARAP in the Peli3 KO livers, suggestive of an inhibition of autophagy (Fig. 2, B and C). Notably, we did not detect any clear alterations in p62 or LC3B lipidation in the livers of Peli3-deficient mice fed on a chow diet, suggesting that the observed phenotypes were starvation dependent (fig. S2G).

The assessment of temporal autophagy dynamics is limited in fixed tissues. To overcome this issue and to gain a more comprehensive understanding of autophagy flux dynamics, we isolated primary hepatocytes from PELI3 KO or WT mice and cultured them in full medium or starved them in the presence or absence of BafA1. These experiments confirmed a block in starvation-induced lipidation of LC3B in Peli3 KO hepatocytes (Fig. 2, E and F). p62 levels were not significantly changed in whole-cell lysates from PELI3 KO hepatocytes (Fig. 2, E and F). To investigate this further, we analyzed the insoluble fractions from the hepatocytes, where we detected p62 at its expected size as well as at higher molecular weight forms, likely reflecting its oligomerization in insoluble aggregates (Fig. 2G) (*36*). The WT hepatocytes displayed an expected clearance of p62 upon induction of autophagy by HBSS treatment, which was partially reversed by BafA1. However, p62 remained elevated in response to starvation in the Peli3 KO hepatocytes, further supporting an abrogated autophagic flux (Fig. 2G). Similar dynamics were observed for total ubiquitin levels in the insoluble fraction (Fig. 2H). Supporting these data, the number of p62 puncta remained elevated after starvation of Peli3-deficient primary hepatocytes in contrast to WT cells (Fig. 2, I and J). Together, these data suggest that Peli3 plays an important role in promoting the autophagic response to starvation in the mouse liver, and that its absence leads to a defect in autophagic flux and a subsequent accumulation of autophagic substrates.

PELI3 is present at autophagic membranes where it binds to LC3/GABARAP proteins

Several core autophagy machinery proteins localize to autophagic membranes where they participate in the regulation of autophagosome formation, expansion, maturation, and fusion (*41*). Because of its regulatory role in autophagy, we asked whether PELI3 may localize at autophagic membranes. To address this, we performed sequential fractionation by differential centrifugation after autophagy induction by starvation and analyzed the supernatants and pellets from the 3000*g* (3K), 25K, and 100K fractions (fig. S3A) (*42*). In contrast to the green fluorescent protein (GFP) control, which was mainly detected in the supernatants, GFP-PELI3 was highly enriched in the 25K and 100K membrane-containing pellets (fig. S3B). To further investigate the nature of the membrane sources, we performed a membrane floatation assay by resolving the membranes on an OptiPrep gradient (Fig. 3A) (*43*). By this method, we found that PELI3 codistributed in the top two light-density fractions together with the highest levels of lipidated LC3B (Fig. 3B). Additionally enriched in these two fractions was the phospholipid-interacting early autophagy initiation factor WIPI2B, suggesting PELI3's presence on early autophagic membranes (Fig. 3B). The enhanced presence of GFP-PELI3 in the middle-density fractions (6 and 7), also positive for the endosomal markers RAB7 and EEA1, suggests that PELI3 may also localize to endolysosomal membranes (Fig. 3B).

Confirming the membrane fractionation results, we found that MYC-PELI3 colocalized with GFP-LC3B at several distinct puncta by immunofluorescence microscopy after starvation (Fig. 3C). Likewise, a similar colocalization was observed between PELI3 and endogenous WIPI2B (Fig. 3D). To investigate whether PELI3 localized within the lumen of autophagic vesicles, we performed a protease protection assay, in which luminal proteins remain protected from proteinase K–mediated digestion (*44*, *45*). PELI3 was not protected from proteinase K digestion, in contrast to known autophagosomal cargo proteins p62 and tax1-binding protein 1 (TAX1BP1), suggesting that Peli3 is not itself a substrate for autophagic degradation during a 2-hour starvation (Fig. 3E). The protease protection assay additionally confirmed that overexpression of MYC-PELI3, relative to a MYC empty vector control, was sufficient to enhance the protection of autophagosomal cargo proteins p62 and TAX1BP1, suggesting PELI3's ability to promote the formation of mature and properly sealed autophagosomes (Fig. 3E).

In Tig3 cells, stably expressing a doxycycline-inducible GFP-tagged PELI3 or a corresponding GFP control, we observed that GFP-PELI3 co-immunoprecipitated (co-IPed) with endogenous LC3B and

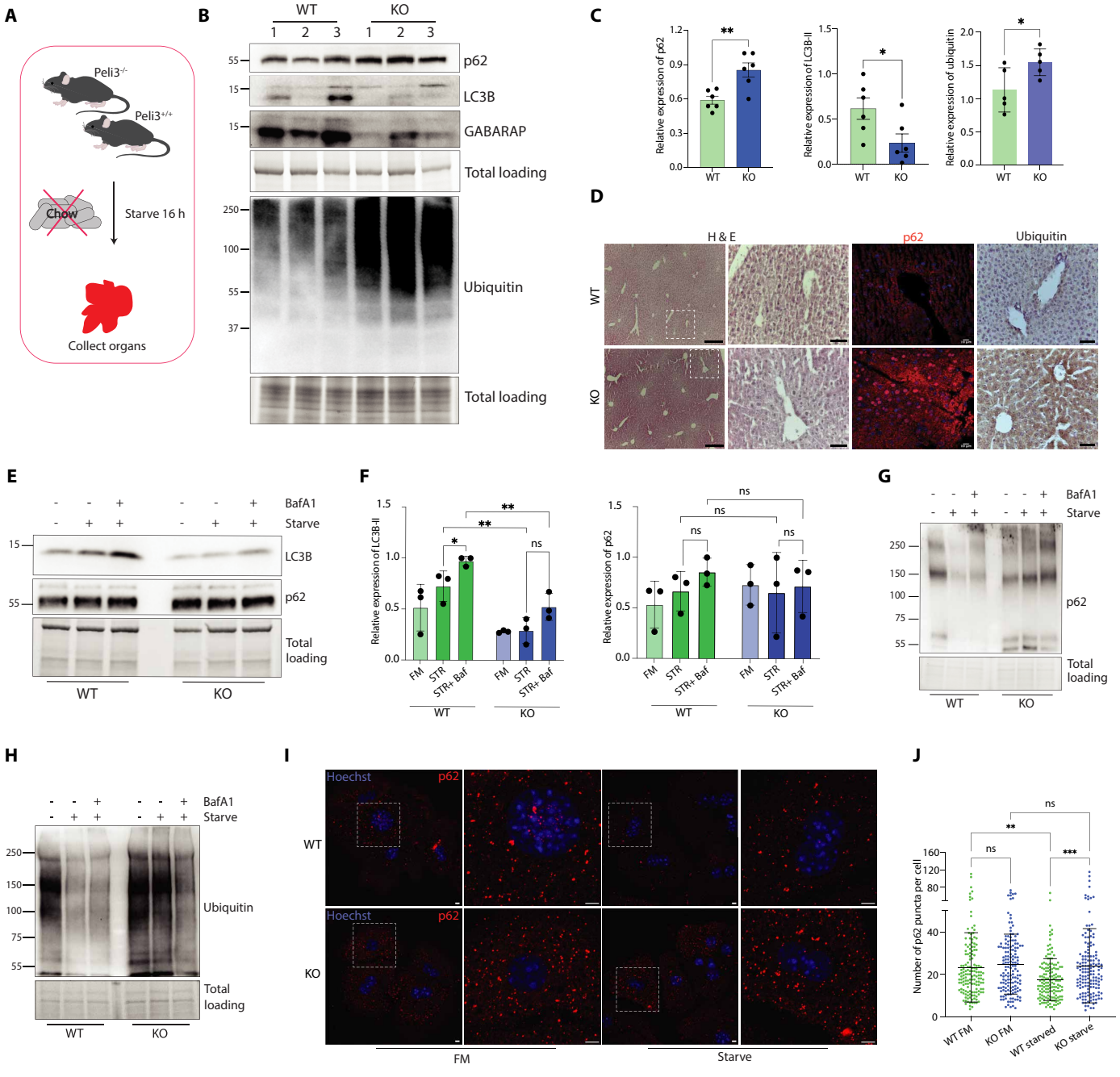

Fig. 2. Starvation-induced autophagy is abrogated in the livers of Peli3-deficient mice. (**A**) Overview of mouse starvation experiments. (**B**) Western blot of liver protein extracts from starved WT and KO mice ($n = 3$). Ubiquitin was run on a separate gel with its corresponding loading control. (**C**) Densiometric quantification relating to (B). Bar graphs depict relative expression of p62, LC3B-II, or ubiquitin normalized to loading. The data represent the mean ± SEM ($n > 5$ mice). Statistical analysis was performed by unpaired Student's *t* test. $*P < 0.05$ and $**P < 0.01$. (**D**) Immunohistochemistry of starved mouse livers stained with H&E, p62, and ubiquitin. Representative images are shown ($n = 3$). Scale bars, 200 μm for widest histological view of H&E stain, 20 μm for magnified H&E inserts and ubiquitin, and 10 μm for p62. (**E**) Representative Western blot of primary hepatocytes from Peli3 WT or KO mice. Starvation and bafilomycin A1 (BafA1) treatments were 4 hours ($n = 4$). (**F**) Densiometric quantification relating to (E). Bar graphs depict mean ± SD of relative expression of LC3B-II and p62 normalized to loading ($n = 3$). Statistical analyses by two-way ANOVA. $*P < 0.05$ and $**P < 0.$ 01. ns, nonsignificant. (**G** and **H**) Representative Western blot analysis of insoluble fractions from primary hepatocytes treated as in (E) ($n = 3$). [(B), (E), (G), and (H)] Gel stain is used as a loading control. (**I**) Primary hepatocytes derived from WT or KO mice cultured in full medium (FM) or starved (HBSS) for 4 hours and immunostained for p62. Representative images (60×) with magnified inserts on the right. Scale bar, 5 μm. [(D) and (I)] Nuclear stain with Hoechst 33342. (**J**) Quantifications relating to (I). Number of p62 puncta/cell quantified from ≥150 cells for each experiment. The data represent mean ± SD ($n = 2$). Statistical analysis was performed by one-way ANOVA. $**P < 0.01$ and $***P < 0.001$.

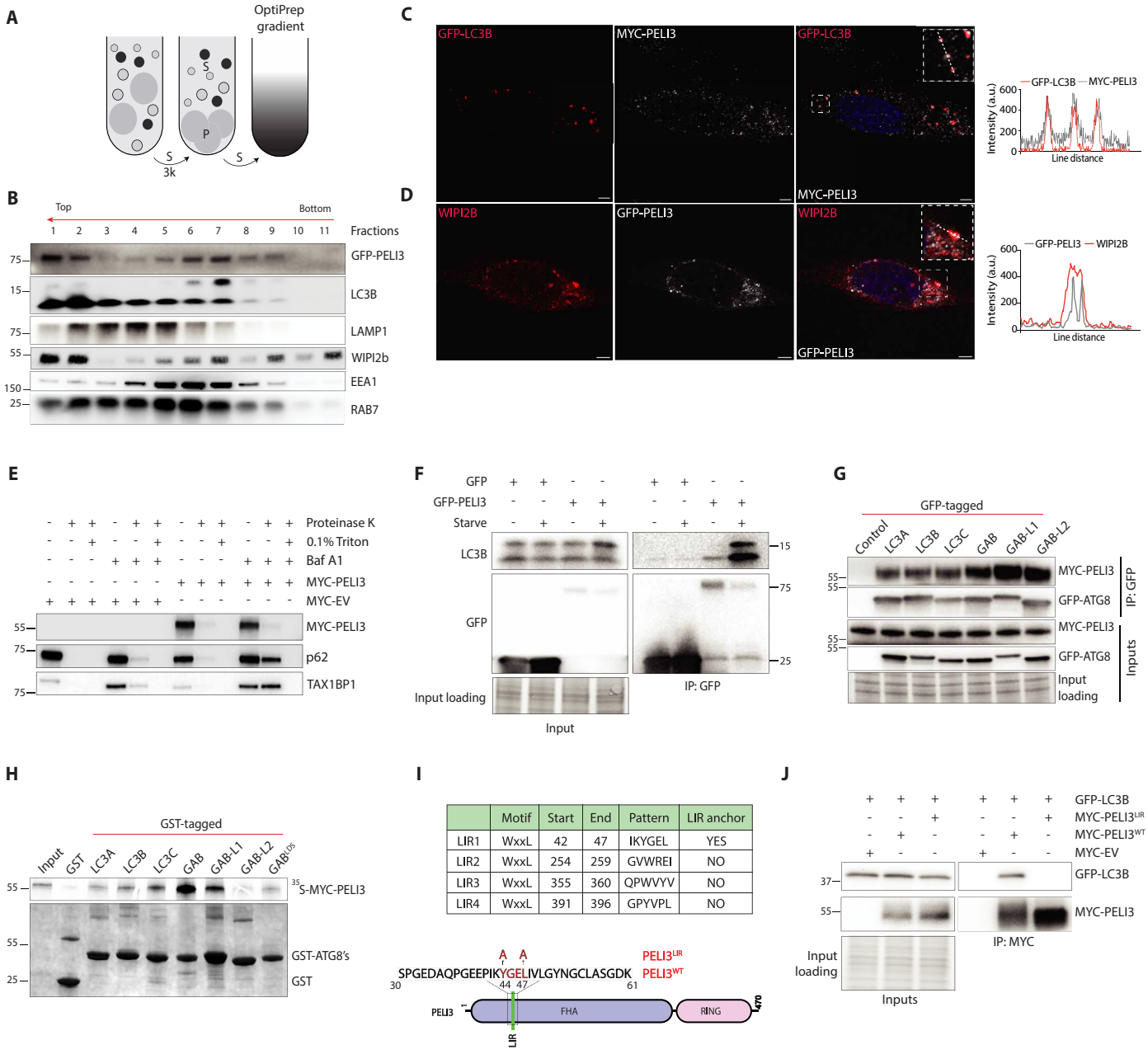

Fig. 3. PELI3 localizes to autophagic membranes and binds to LC3/GABARAP proteins via a LIR domain. (**A**) Schematic of density gradient fractionation and membrane floatation assay by OptiPrep gradient. P, pellet; S, supernatant. (**B**) Tig3 cells expressing GFP-PELI3 (starvation and BafA1, 2 hours) analyzed by membrane floatation assay (A). Protein lysates from indicated fractions were subjected to Western blotting. A representative experiment is shown ($n = 2$). (**C** and **D**) Confocal microscopy analysis of GFP-LC3B and MYC-PELI3 (C) or endogenous WIPI2B and GFP-PELI3 (D) in HeLa cells treated as in (B). Scale bars, 5 μm. Line scans indicate the degree of colocalization between proteins of interest (magnified inserts, top right). Intensity profiles (right) are presented as arbitrary units (a.u.). (**E**) HEK293T cells expressing MYC-EV or MYC-PELI3 were treated with dimethyl sulfoxide (DMSO) or BafA1 for 2 hours. A protease protection assay was performed (see Materials and Methods), and lysates were subjected to Western blotting. A representative experiment is shown ($n = 3$). (**F** and **G**) Co-IP from Tig3 cells expressing GFP or GFP-PELI3 in full medium or starved (HBSS, 2 hours) (F) or from HEK293T cells expressing indicated GFP-tagged ATG8s and MYC-PELI3 (G). Western blot analysis of inputs and IP fractions from a representative experiment ($n = 3$). (**H**) GST pulldowns of radiolabeled (^{35}S) MYC-PELI3 with indicated GST-ATG8s. GAB^{LDS} (LIR docking site mutant). A representative experiment is shown ($n = 2$). (**I**) Top: Features of four potential LIR motifs in PELI3 predicted by iLIR. Bottom: Schematic representation of PELI3 domain composition and experimentally identified LIR motif. Highlighted in red is the LIR motif and the mutational strategy for generating the mutant PELI3^{LIR}. (**J**) Co-IP from HEK293T cells expressing GFP-LC3B with MYC-PELI3 ^{WT}, MYC-PELI3^{LIR} (LIR mutant), or MYC-EV (empty vector). Western blot of input and IP are shown from a representative experiment ($n = 3$). [(F), (G), and (J)] Gel stain is used as a loading control.

that this interaction was enhanced after 2-hour starvation (Fig. 3F). PELI3 consists of an N-terminal forkhead associated domain (FHA) and a C-terminal RING domain that mediates substrate ubiquitination (*46*). Both the FHA and RING domains alone displayed a reduced binding to LC3B, relative to the full-length PELI3, suggesting that both parts of the protein contribute to LC3B binding (fig. S3C). Because LC3B belongs to a family of six different ATG8 proteins, we investigated the ability of PELI3 to bind to each of these. By co-IP of GFP-tagged ATG8 proteins transiently expressed in human embryonic kidney (HEK) 293T cells, we found that MYC-PELI3 interacted with all six ATG8s, albeit with the strongest interactions among the GABARAP family members (Fig. 3G).

Assessing this in vitro through pull-downs of glutathione *S*-transferase (GST)–tagged ATG8s confirmed that this binding was direct, and except for GABARAPL2 that showed a weak interaction in the in vitro assay, these experiments confirmed a similar trend as the co-IPs (Fig. 3H). An LDS (LIR motif docking site) mutated version of GABARAP displayed a strongly reduced interaction with PELI3 relative to WT GABARAP (Fig. 3H), suggesting that PELI3 interacts with ATG8 family members through a canonical LIR motif.

We analyzed the PELI3 amino acid sequence for the presence of a potential LIR motif based on established criteria (*47*), additionally considering recent indications that a >3-residue overlap with an intrinsically disordered region, as predicted by ANCHOR software, may increase the potential for stabilization upon binding to a target molecule (*48*). Among four predicted LIRs, only one site fulfilled the anchor criteria, located in the N-terminal region within the Peli3 FHA domain (Fig. 3I). Mutation of two residues in this motif ($PELI3^{LIR}$) led to a strongly reduced interaction with LC3B, as well as with GABARAP (Fig. 3, I and J, and fig. S3D). Further confirming the functionality of this site, we observed a reduced recruitment of $PELI3^{LIR}$ to the 25K membrane-containing pellet, relative to the $PELI3^{WT}$ or a PELI3 mutant deficient of E3 ligase activity, $PELI3^{E3}$ (fig. S3E) (*25*). The LIR mutation in PELI3 did not reduce the stability of the protein or alter its ability to bind to its known interaction partner TRAF6 (fig. S3F) (*38*).

Depletion of PELI3 leads to the accumulation, mislocalization, and reduced activity of ULK1

In our initial screen validation experiments, we noted a consistent up-regulation of ULK1 protein levels upon Peli3 depletion in starved Tig3 cells (fig. S1, F to H). Moreover, our data indicate that PELI3 functions at a relatively early step of autophagosome formation. ULK1 is the immediate upstream kinase that acts as a bridge between nutrient sensing and induction of the autophagic response (*49*). The timely degradation of ULK1 is required to maintain proper oscillations of autophagy during starvation, and abnormally increased levels of ULK1 can inhibit autophagy (*22*, *50*). Assessing ULK1 levels further in Tig3 cells, we found that while ULK1 undergoes a time-dependent decrease during a starvation time course, this was clearly abrogated after siRNA-mediated depletion of PELI3 (Fig. 4, A and B). Similar findings in a cycloheximide chase assay suggested that ULK1 was stabilized posttranslationally in the absence of PELI3 (Fig. 4, C and D). We next asked whether the abrogated autophagic flux in the livers of Peli3-deficient mice (Fig. 2) could be related to alterations in ULK1 levels. We detected significantly increased ULK1 expression levels in the livers of starved Peli3 KO relative to WT mice, as determined by Western blotting (Fig. 4, E and F) and by immunohistochemistry (Fig. 4G). Of note, there were no changes in ULK1 expression in livers from mice fed on a standard chow diet (fig. S4A), which also did not display any overt defects in autophagy (fig. S2G). Despite the increase in total ULK1 expression levels, Peli3 KO cells displayed significantly fewer ULK1 puncta in response to starvation while simultaneously presenting with an aberrant accumulation of ULK1 into larger cytoplasmic deposits, together suggesting its potential mislocalization away from canonical autophagy initiation sites (Fig. 4, H and I). To understand whether this could affect ULK1's ability to phosphorylate its downstream targets for autophagy initiation, we determined the phosphorylation status of the ULK1 substrate ATG14. We found that despite an accumulation of ULK1 in Peli3 KO hepatocytes, the starvation-induced phosphorylation of ATG14 on Ser^{29} by ULK1 was significantly reduced (Fig. 4, J and K). A similar trend was observed in the liver tissues (fig. S4, B and C). The mTORC1-mediated inhibitory phosphorylation on ULK1 Ser^{757} (*51*) was not enhanced, suggesting that the decrease in ULK1 activity was not due to its upstream inhibition through mTORC1 signaling (Fig. 4J and fig. S4B). Likewise, there were no marked changes in phosphorylated ribosomal protein S6 kinase (P-S6K) or phosphorylated AMP-activated protein kinase (P-AMPK) levels in the livers of Peli3 KO mice (fig. S4D). Together, these data suggest that depletion of PELI3 leads to the stabilization, accumulation, and mislocalization of ULK1 during starvation. This results in a reduction of ULK1-mediated phosphorylation of ATG14, likely due to its reduced presence at canonical autophagy initiation sites, contributing to a global decrease in autophagy.

PELI3 forms a complex with ULK1 to promote its ubiquitination and proteasomal degradation

To address whether ULK1 may be a substrate of PELI3, we first assessed whether they interact. Following transient coexpression of tagged PELI3 and ULK1 constructs in HEK293T cells and co-IPs in both directions, we found a clear interaction between these proteins (fig. S5, A and B). We validated this interaction with endogenous ULK1 in Tig3 cells by stably expressing GFP-PELI3 or a corresponding GFP vector control and found that the interaction was enhanced in response to starvation (Fig. 5A). Co-IPs with a panel of ULK1 truncations revealed that the mid- and C-terminal regions of ULK1 were important for the interaction with PELI3. A short extension of the ULK1 N-terminal region, allowing inclusion of the ULK1 LIR domain (*52*), was also sufficient to retain binding to PELI3 (Fig. 5B). Reverse co-IPs with truncations of PELI3 showed that the FHA domain of PELI3 was sufficient to bind ULK1, albeit with a lower efficiency than the full-length PELI3 (PELI3-FL), while the RING domain alone did not bind to ULK1 (Fig. 5C). Since the PELI3 FHA domain contains the PELI3 LIR motif (Fig. 3I), we investigated the interaction between the MYC-$Peli3^{LIR}$ mutant and hemagglutinin (HA)–ULK1, which we found to be clearly reduced, suggesting that PELI3's binding to ATG8 proteins is important for its recruitment to ULK1 (Fig. 5D). Supporting these data, MYC-PELI3 colocalized with endogenous ULK1 after starvation, at puncta that also colocalize with GFP-LC3B (fig. S5C).

Since PELI3 binds to ULK1 and since its absence promotes ULK1 stability, we speculated whether PELI3 can ubiquitinate ULK1 to regulate its turnover. IP of ULK1 followed by analysis of its ubiquitination status after expression of GFP-PELI3 or GFP alone suggested that PELI3 primarily mediates K48-linked ubiquitination of ULK1 (fig. S5D). This was only induced by WT PELI3 ($PELI3^{WT}$), while the

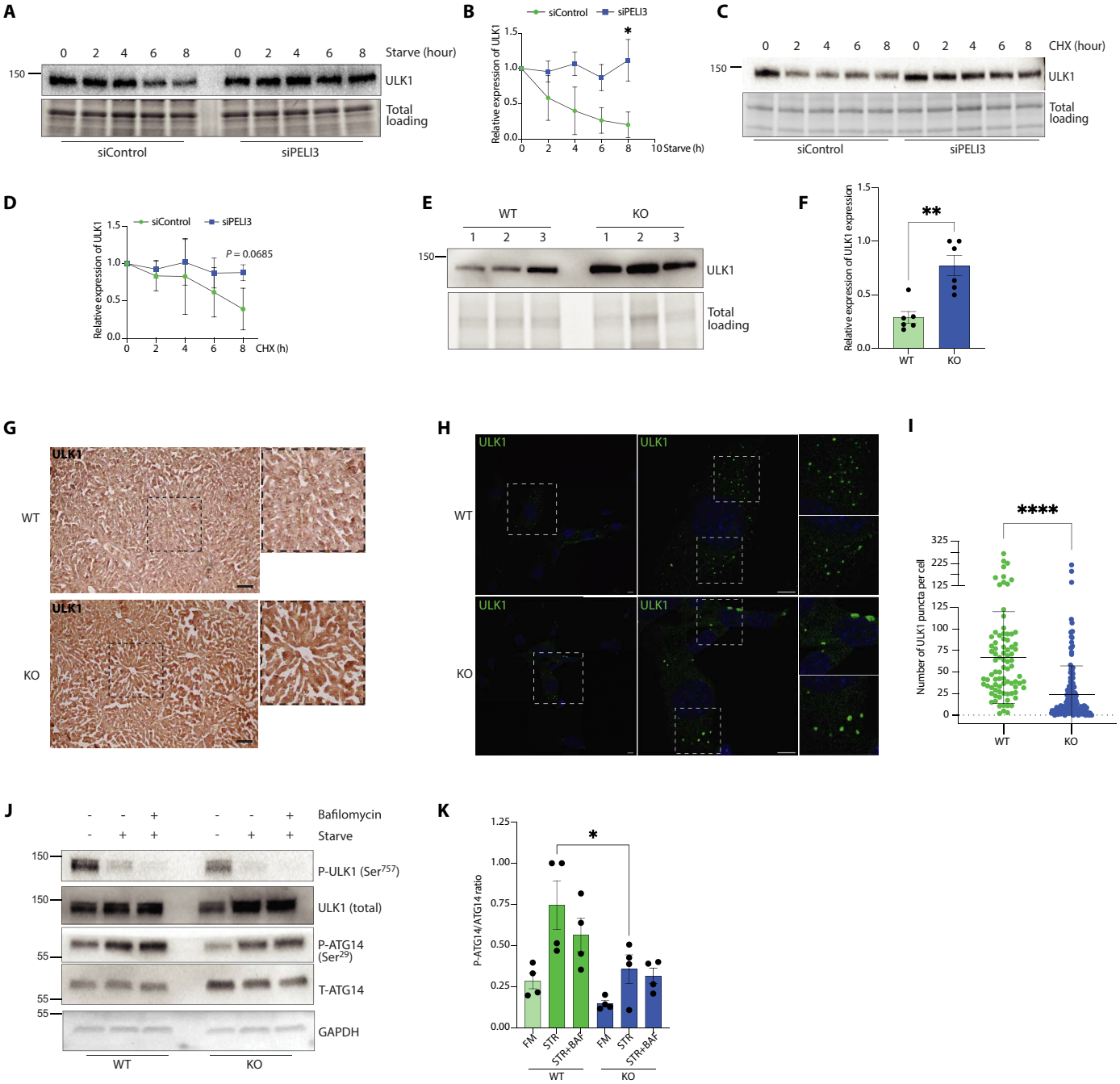

Fig. 4. Depletion of PELI3 leads to the aberrant accumulation of ULK1. (**A** and **C**) Tig3 cells (72-hour transfection) were starved for indicated intervals in HBSS (A) or starved for 16 hours before treatment with cycloheximide (CHX) (100 ng/ml) for indicated intervals (C). A representative Western blot is shown ($n = 3$). (**B** and **D**) Densiometric quantifications relating to (A) and (C). Data represent relative ULK1 expression normalized to time point zero and total loading and are depicted as the mean ± SEM from three independent experiments. Statistical analysis was performed by two-way ANOVA. $^{*}P < 0.05$ (B) and $P = 0.0685$ (D). (**E**) Western blot of liver tissue lysates from starved WT and KO mice. A representative blot from three mice of each genotype is shown. [(A), (C), and (E)] Gel stain is used as a loading control. (**F**) Densiometric quantification relating to (E). The graph depicts relative expression of ULK1 normalized to total loading. The data represent mean ± SD ($n = 6$). Statistical analysis was performed by unpaired Student's *t* test. $^{**}P < 0.01$. (**G**) Representative images from immunohistochemistry of starved mouse livers stained for ULK1. Scale bar 100 μm. (**H**) Representative images (60×) of WT and Peli3 KO cells starved for 2 hours in HBSS and immunostained for ULK1. Nuclear stain with Hoechst 33342. Magnified inserts shown on the right. Scale bar, 5 μm. (**I**) Quantifications relating to (H). ULK1 puncta quantified from ≥120 cells. Data represent the mean ± SD from three independent experiments. Statistical analysis was performed by unpaired Student's *t* test. $^{****}P < 0.0001$. (**J**) Representative Western blot of primary hepatocytes from Peli3 WT and KO mice. Starvation and BafA1 treatments were for 4 hours ($n = 3$). (**K**) Densiometric quantification of phospho-ATG14 (P-ATG14) (Ser^{29}) and total ATG14 (T-ATG14) relating to (J). Data depict the mean ± SD from four independent experiments. Statistical analyses by one-way ANOVA. $^{*}P < 0.05$.

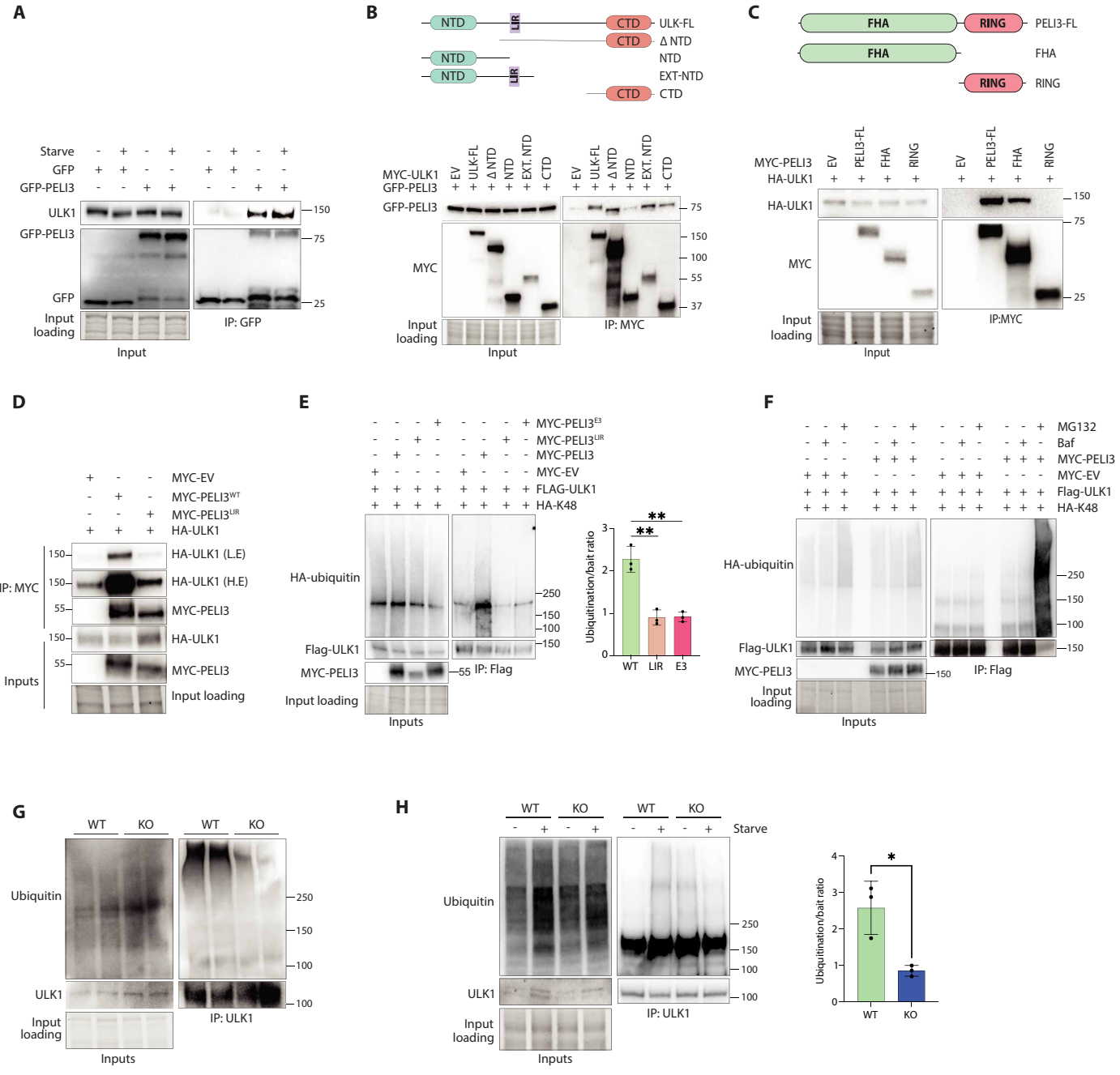

Fig. 5. PELI3 binds to and ubiquitinates ULK1, leading to its proteasomal degradation. (**A**) Co-IP from Tig3 cells expressing GFP or GFP-PELI3 in full medium or starved (HBSS, 2 hours). Western blot of inputs and IP fractions are shown from a representative experiment ($n = 3$). (**B** and **C**) Top: Schematic of ULK1 (B) or PELI3 (C) domain organization and relevant deletion constructs. Bottom: Co-IP from HEK293T cells expressing indicated constructs. Western blot analysis of inputs and IP fractions are shown from a representative experiment ($n = 3$). (**D**) Co-IP from HEK293T cells expressing indicated constructs. Western blot analysis of inputs and IP fractions are shown from a representative experiment ($n = 3$). L.E, low exposure; H.E, high exposure. (**E**) Left: Co-IP from HEK293T cells expressing indicated constructs. Western blot analysis of inputs and IP fractions are shown from a representative experiment ($n = 3$). Right: Corresponding densiometric quantification of ubiquitin levels normalized to bait. The data represent mean ± SD ($n = 3$). Statistical analysis performed by unpaired Student's t test. $^{**}P < 0.01$. (**F**) Co-IP from HEK293T cells expressing indicated constructs and treated with BafA1 or MG132 as indicated (2 hours). Western blot analysis of inputs and IP fractions are shown from a representative experiment ($n = 3$). (**G**) Co-IP of endogenous ULK1 from starved WT and Peli3 KO mouse liver tissue. Western blot analysis of inputs and IP fractions are shown from a representative experiment ($n = 3$). (**H**) Left: Co-IP of endogenous ULK1 from WT and Peli3 KO mouse-derived primary hepatocytes in full medium or starved. Western blot analysis of inputs and IP fractions are shown from a representative experiment ($n = 3$). Right: Corresponding densiometric quantification of ubiquitin levels normalized to bait from starved samples. The data represent mean ± SD ($n = 3$). Statistical analysis performed by unpaired Student's t test. $^{*}P < 0.05$.

PELI3^{E3} mutant failed to do so (Fig. 5E). This suggests the dependency on the intrinsic activity of PELI3 for promoting ULK1 ubiquitination. The PELI3^{LIR} mutant was also unable to ubiquitinate ULK1 (Fig. 5E), suggesting that PELI3's binding to ATG8 proteins can facilitate its ubiquitination of ULK1, potentially by mediating its correct positioning at autophagic membranes. Supporting the role of the ATG8s as facilitators of the PELI3-ULK1 interaction, HeLa cells lacking all six ATG8 proteins (Hexa KO) displayed a reduced interaction between PELI3 and ULK1 relative to corresponding control cells (fig. S5E). Moreover, PELI3-mediated ubiquitination and degradation of ULK1 was clearly also reduced in the Hexa KO cells (fig. S5, F and G). We found that PELI3 did not ubiquitinate the ATG8 proteins themselves (fig. S5H). Both the interaction between PELI3 and ULK1, as well as the PELI3-mediated ubiquitination of ULK1 were clearly increased by MG132 treatment, suggesting that PELI3-mediated ubiquitination of ULK1 leads to its degradation by the proteasome (fig. S5I and Fig. 5F). To substantiate these data in a physiological context, we immunoprecipitated endogenous ULK1 from mouse-derived liver tissues and from primary hepatocytes and assessed ULK1's ubiquitination status in the presence or absence of Peli3. We found that the levels of endogenous ubiquitinated ULK1 were reduced in liver tissue derived from starved Peli3 KO relative to WT mice (Fig. 5G). Comparison of full medium and starvation conditions in primary hepatocytes revealed that while basal ULK1 ubiquitination levels were mildly enhanced in Peli3 KO cells grown in full medium, the starvation-dependent increase in ULK1 ubiquitination was abolished in the absence of Peli3 (Fig. 5H). In sum, the data suggest that in the context of starvation in cells and in mouse liver, PELI3 ubiquitinates ULK1, leading to ULK1's degradation by the proteasome. In absence of PELI3, ULK1 is stabilized, leading to its aberrant accumulation, mislocalization, and hence reduced activation of starvation-induced autophagy.

Peli3 regulates hepatic lipid stores in vivo through autophagy

The livers from starved Peli3 KO mice showed a pronounced hepatocyte swelling, as well as an increase in steatotic areas devoid of staining (Fig. 6A). A BODIPY stain was used to assess the content of LDs, known to be a major autophagic substrate in the liver in response to starvation. We detected a clear accumulation of LDs in Peli3 KO relative to WT livers derived from mice subjected to 16-hour starvation (Fig. 6B). This phenotype was additionally confirmed with a Nile red stain (fig. S6A). TEM analysis of the livers demonstrated both an increase in the amount and size of LDs when Peli3 was ablated (Fig. 6C). To further confirm these alterations, liver homogenates were subjected to mass spectrometry–based shotgun lipidomics to determine the absolute quantities of triacylglyceride (TAG) and cholesterol ester (CE) storage lipids, which are the main components of LDs (*53*). The analysis revealed a significant increase in the abundance of total TAGs in livers of starved KO mice in comparison to WT (Fig. 6D). Further investigation of individual TAG species revealed the most significant differences within the subgroup of TAG species with total acyl carbon atoms between 50 and 56 (fig. S6B). The CE content was similarly increased in the Peli3 KO mouse livers (Fig. 6D), although the total CE abundance was generally lower than the TAGs in mice of both genotypes.

To investigate the starvation response dynamics as well as the underlying cause of LD accumulation in more detail, we turned to the mouse-derived primary hepatocytes. The BODIPY signal was weak in hepatocytes cultured in full medium; however, the signal was clearly enhanced in response to starvation (Fig. 6E). Here, Peli3 KO hepatocytes presented with a significant increase in the number of LDs per cell, as well as an enhanced mean LD size, in comparison to WT cells (Fig. 6, E and F). The extent of LD processing by the autophagic system is commonly estimated by a quantification of the proximity between LDs and lysosomes (*8*, *54*). By costaining for the lysosomal marker lysosome-associated membrane protein 2 (LAMP2) and BODIPY, we observed a significant decrease in the proximity between lysosomes and LDs in Peli3 KO hepatocytes (Fig. 6, G and H). This suggests that the accumulation of LDs, as well as their enhanced size may be related to a decreased capacity for their lysosomal digestion. Further supporting this, we observed a decreased presence of LDs in the vicinity of and/or engulfed by autophagic vesicles in Peli3 KO liver tissue by TEM analysis, suggesting a decreased uptake of LDs by the autophagic-lysosomal system (Fig. 6, I and J, and fig. S6C). Together, these data suggest that deletion of Peli3 worsens starvation-induced hepatic steatosis in mice due to defective autophagic processing of LDs.

Hepatic steatosis in humans is a common pathological feature shared within a large group of diseases classified under the term MASLD. To explore the potential implications for PELI3 in hepatic steatosis in humans, we compiled and analyzed gene expression data from a collection of MASLD patients relative to control samples (*55*, *56*). We found *PELI3* expression levels to be significantly decreased in MASLD (Fig. 6K), suggesting a potential role for *PELI3* in MASLD-associated hepatic steatosis in humans. Moreover, a single sample gene set enrichment analysis (ssGSEA) using curated lists of autophagy genes (table S3) suggested a significant decrease in autophagy gene expression, and thus an overall reduction in autophagy levels in the MASLD samples (fig. S6, D and E).

DISCUSSION

The dynamic nature of the autophagy response poses the requirement for tightly regulated fine-tuning of the autophagy machinery proteins at several levels. This includes their localization, activity, and interaction networks, but additionally involves the constant adjustment of their steady-state protein levels (*5*, *41*). Major players in this regard include E3 ubiquitin ligases, which target their substrates for ubiquitin-mediated degradation, either by autophagy itself or by the proteasome (*20*, *21*, *23*, *24*).

Here, we identify the E3 ligase PELI3 as a crucial regulator of starvation-induced autophagy. We find that PELI3 is recruited to autophagic membranes in response to starvation, where it binds directly to LC3/GABARAP proteins. This in turn facilitates PELI3's binding to and ubiquitination of ULK1. We show that PELI3-mediated K48-linked polyubiquitination of ULK1 leads to its degradation by the proteasome, comprising an important step in the control ULK1 levels during starvation (Fig. 7). As ULK1 is a positive regulator of autophagy, it may at first glance seem counterintuitive that its degradation is required for autophagosome formation. However, it is known that ULK1 levels continuously oscillate and that enhanced levels of ULK1 have an inhibitory effect on autophagy (*22*, *50*). Beyond ULK1, it is similarly known that overexpression of other core components of the autophagic machinery, including ATG12 and ATG16L1, leads to a potent autophagy inhibition (*24*, *57*). While the exact cause of this remains unknown, this is likely due to the formation of incomplete or nonfunctional complexes caused by unbalanced subunit stoichiometry, protein mislocalization, and/or aggregation into abnormal structures. In line with this,

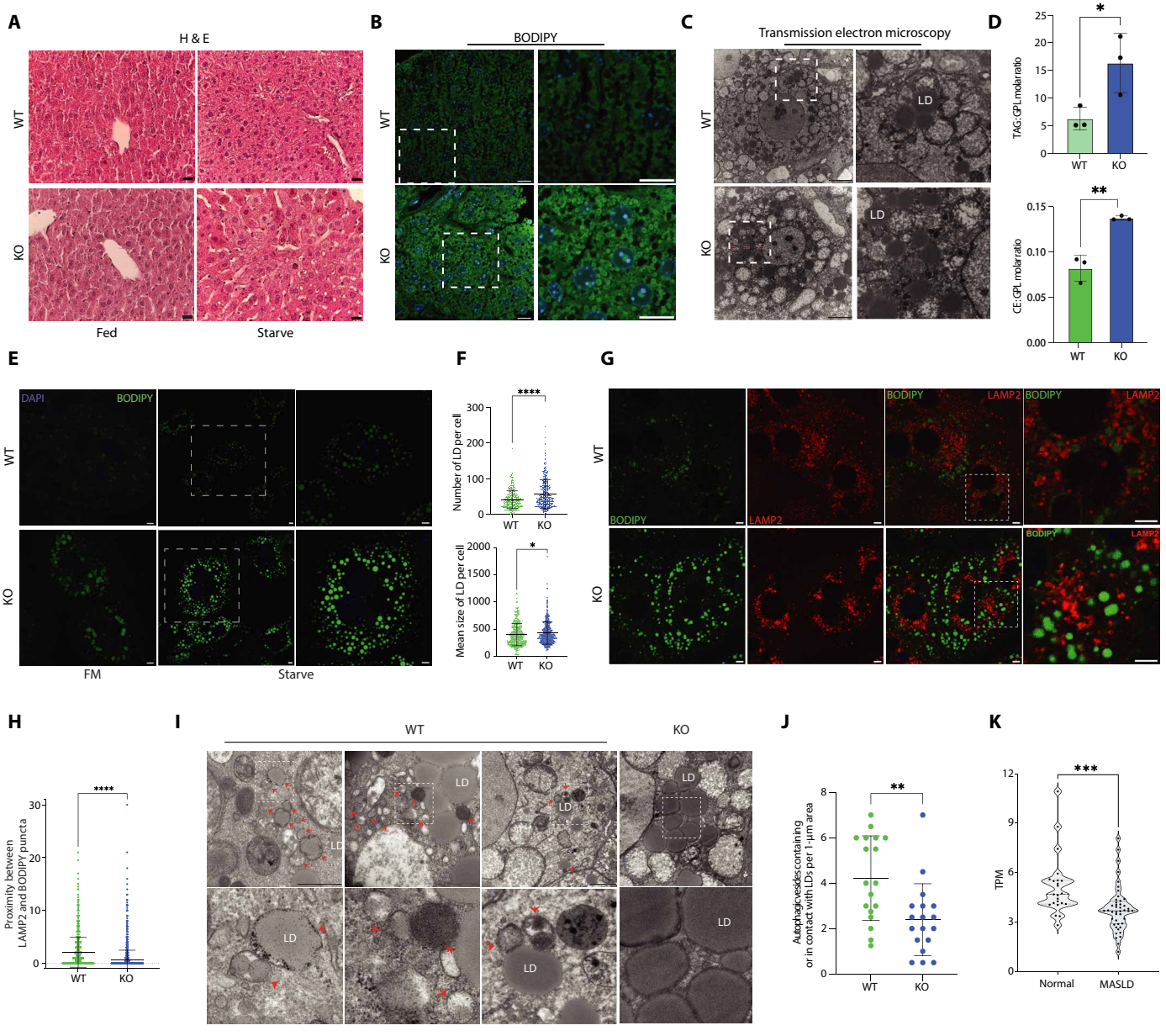

Fig. 6. Peli3 deletion enhances starvation-induced hepatic steatosis by disrupting autophagic turnover of lipid droplets. (**A** to **C**) Representative images from starved mouse liver sections stained with H&E (A) and BODIPY (B) or fixed and processed for TEM (C). Scale bars, 20 µm ($n = 10$) (A), 20 µm ($n = 3$) (B), and 5 µm ($n = 2$) (C). LD, lipid droplet. (**D**) Triacylglycerol (TAG) and cholesteryl ester (CE) levels in starved mouse liver homogenates normalized to total level of GPLs determined by shotgun lipidomics. Data represent mean ± SD ($n = 3$), unpaired Student's t test. $^{*}P < 0.05$ and $^{**}P < 0.01$. (**E** and **G**) Representative (60×) images of primary hepatocytes in full medium (FM) or starved (16 hours) (E) or starved (16 hours) + BafA1 for the last 4 hours (G). Cells stained as indicated with BODIPY (green), LAMP2 antibody (red), and Hoechst 33342. Scale bars, 5 µm (magnified inserts on the right). (**F**) Quantification related to (E). The mean ± SD for number and size of BODIPY puncta/cell from ≥140 starved cells from each experiment ($n = 2$). (**H**) Quantification related to (G). Nearest-neighbor analysis counts the number of LAMP2 objects adjacent (<5-pixel proximity) to each BODIPY object. Quantifications from ≥140 cells; mean proximity ± SD is shown ($n = 2$). [(F) and (H)] Unpaired Student's t test. $^{*}P < 0.1$ and $^{****}P < 0.0001$. (**I**) Representative TEM images (mouse liver, 16-hour starvation). Magnified inserts (bottom). Red arrows depict autophagic/lysosomal vesicles in contact with/containing LDs. Scale bars, 1 or 2 µm. (**J**) Quantification relating to (I). Mean number of autophagic/lysosomal vesicles in contact with/containing LDs ± SD per 1-µm area ($n = 2$). Unpaired Student's t test. $^{**}P < 0.01$. (**K**) Peli3 mRNA expression in 23 livers from healthy individuals and 44 livers from MASLD patients. Dunn's multiple comparisons test $^{***}P < 0.001$. TPM, transcripts per million.

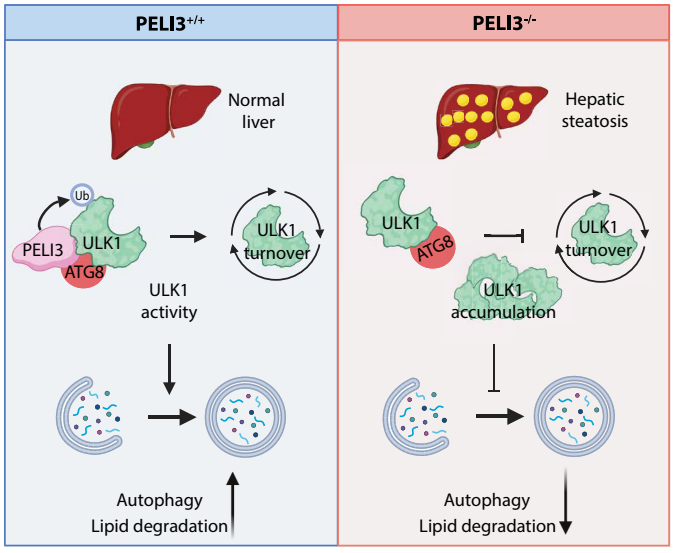

Fig. 7. PELI3 regulates autophagy and lipid homeostasis. In response to nutrient deprivation, PELI3 safeguards ULK1 homeostasis through ubiquitination of ULK1. This is facilitated by PELI3's interaction with ATG8 proteins. In the absence of PELI3, ULK1 accumulates, leading to a disruption of autophagy and a decreased degradation of LDs in the liver, causing enhanced hepatic steatosis. Created with BioRender (Frankel, 2023; https://BioRender.com/a71f180).

the data presented here suggest that in absence of Peli3, ULK1's accumulation and mislocalization reduce its availability at canonical autophagy initiation sites, leading to a defect in starvation-induced autophagosome formation both in cells and in the mouse liver (Fig. 7).

We found that the PELI3 LIR mutant displayed a decreased membrane recruitment and a reduced binding to LC3/GABARAP (ATG8) proteins, as well as an inability to bind to and ubiquitinate ULK1. The data therefore suggest that PELI3 may be correctly positioned at autophagic membranes, at least in part, through its binding to ATG8 proteins. This would in turn allow it to complex with ULK1 and target it for degradation during nutrient deprivation. In support of this finding, the LC3/GABARAP proteins have previously been suggested to act as scaffolds for the assembly of autophagy complexes, by facilitating or maintaining their attachment to the phagophore surface (*58*). Since deletion of the C-terminal RING domain also reduced PELI3's binding to LC3B, it is possible that additional determinants or binding partners may facilitate this interaction. Hexa KO cells lacking all six ATG8 proteins displayed a diminished interaction between PELI3 and ULK1, supporting the importance of ATG8 in facilitating the interaction while also suggesting the potential involvement of additional factors.

PELI3 is a member of the Pellino protein family composed of PELI1, PELI2, and PELI3, all of which contain an N-terminal FHA- and a C-terminal RING-like domain with E3 ligase activity (*46*). These proteins are versatile regulators in innate immune signaling, yet despite their structural similarities, the individual family members are involved in distinct signaling pathways (*59*, *60*). In line with this, depletion of PELI1 or PELI2 did not affect autophagy (table S1), suggesting the functional specificity of PELI3 in this context. PELI3 itself was previously suggested to be an autophagy substrate in the context of lipopolysaccharide (LPS) treatment (*61*). However, we did not observe any protection of Peli3 in protease protection experiments, in contrast to the known cargo proteins p62 and TAX1BP1, suggesting that Peli3 is not located within the autophagosome lumen under conditions of starvation. PELI3 may rather exert its functions at the outer limiting membrane of autophagic structures; however, the precise details of its positioning remain to be elucidated. It is also noteworthy that both the colocalization and fractionation data clearly suggested that beyond autophagic vesicles, Peli3 likely localizes at additional intracellular membranes, including endosomes. This suggests potential broader functions of PELI3 in vesicular trafficking and membrane dynamics.

Different types of cargo degraded by autophagy can include organelles, aggregates, pathogens, and lipids (*62*–*64*). While cargo specification can be directed through signals for selective autophagy, cargo preference is also influenced by the nature of the tissue in question. In response to long-term starvation, enhanced fatty acid uptake by the liver leads to an accumulation of surplus lipids within LDs (*65*). This phenomenon is conserved from flies to humans and, like overfeeding, can lead to lipotoxicity and liver atrophy. LDs therefore encompass a major autophagy substrate in hepatocytes during starvation, the breakdown of which plays a vital role in fulfilling energy demands (*8*, *66*). Defects in ULK1 function, including its reduced ability to phosphorylate ATG14, were previously implicated in the development of hepatic steatosis (*67*). Supporting this, our study demonstrates that fasting-induced hepatic steatosis in mice is exacerbated in the absence of Peli3 and that this can be attributed, at least in part, to dysregulation of ULK1 and autophagic malfunction. While a potentially more specific role for ULK1 in the degradation of LDs cannot be excluded, our data rather suggest that Peli3's role in regulating early steps of starvation-induced bulk autophagy would affect the degradation of multiple substrates, including LDs. Peli3 was previously suggested to protect against obesity-induced inflammation with an impact on hepatic steatosis, although the mechanism linking Peli3 to lipid homeostasis remained unclear (*38*). Together with our findings, this suggests consistent effects of Peli3 in the liver independent of the model or initiating stimulus. Comparatively, inhibition of autophagy through depletion of ATG7, ATG14, or transcription factor EB (TFEB) also enhanced starvation-induced hepatic steatosis (*8*, *68*, *69*). However, independent reports of an opposite phenotype also exist (*36*, *70*), underlining complexities in autophagy dynamics or potential autophagy-independent effects. Hepatic steatosis is the central pathological hallmark in the chronic liver disease MASLD. This umbrella term, previously recognized as nonalcoholic fatty liver disease (NAFLD), encompasses a variety of different conditions associated with LD accumulation in the liver with varying etiologies including unhealthy diet, high-fat diet, or malnutrition (*71*). Autophagy impairment is implicated in the development and progression of MASLD, and pharmacological treatments that enhance autophagic flux have shown promising results by alleviating hepatic steatosis in mice (*72*, *73*). We found Peli3 expression levels to be significantly decreased in livers of MASLD patients relative to healthy controls, suggesting a potential contribution to the underlying disease pathology.

Together, we reveal a critical regulatory layer for starvation-induced tuning of ULK1 protein levels to facilitate the early steps of autophagosome formation. The physiological importance of this mechanism is substantiated by the consequences of Peli3 ablation in mice as well as by alterations in Peli3 expression from MASLD patients. On the basis of these findings, we propose a critical role for Peli3 in the control of liver lipid metabolism through autophagy, suggesting its protective role in liver health.

MATERIALS AND METHODS

Mice

The Peli3$^{-/-}$ mouse line C57BL/6N-Peli3<tm1b(KOMP)Mbp>/Tcp was generated at The Toronto Centre for Phenogenomics (TCP) and obtained from the Canadian Mouse Mutant Repository. The repository was made as part of the KOMP2-DTCC project from KOMP ES cells (*74*). Briefly, Peli3$^{-/-}$ mice were generated by crossing mice holding the tm1a allele with a constitutive Cre-expressing mouse line. Recombination of loxP sites results in the tm1b allele removing the loxP flanked critical exon 3 found in all isoforms of Peli3 (fig. S2A). A frameshift is introduced producing a null allele (Peli3$^{-/-}$). Mice were genotyped by PCR analysis of DNA isolated from ear punches using primers WT-F: AGCAGCAATCAAGGCAATGGCTCACC, WT-R: ACAAGTCAAGCACACACAAGGCCCAG, KO-F: CCATTACCAGTTGGTCTGGTGTC, KO-R: ATCACATCCCACTCTTGGAGCGTTG, Control-F: CACCGGAGAATGGGAAGCCGAA, and Control-R: TCCACACAGATGGAGCGTCCAG. To assess autophagy, mice were separated into individual cages and starved overnight with access to water for 16 hours. The next day, tissues were harvested and processed for experiments. Mice were housed at the animal facility at the Danish Cancer Institute (Copenhagen, Denmark), approval number 2023-15-0206-00074. Mice experiments were approved by the Danish animal experiments inspectorate (Dyreforsøgstilsynet, 2023-15-0201-01392).

MEF isolation

MEFs were isolated as previously described (*75*). Briefly, 6 to 10 Peli3 KO or WT mouse embryos of undetermined sex were aseptically dissected at embryonic day 13.5. Heads and internal organs were discarded; bodies were rinsed twice with phosphate-buffered saline (PBS) and thoroughly minced using a razor blade, and cells were dissociated by incubating in 10 ml of 0.05% trypsin-EDTA at 37°C for 5 min, followed by neutralization of trypsin by addition of fresh Dulbecco's modified Eagle's medium (DMEM) containing L-glutamine, penicillin-streptomycin, and fetal bovine serum (FBS). Cells were pelleted by centrifugation at 200*g* for 5 min, and the cells were washed again with fresh medium, plated on 150-mm plastic culture dishes, and incubated at 37°C with 5% CO_2.

Mouse primary hepatocyte isolation

Peli3 KO or WT mice were anesthetized via intraperitoneal injection of avertin, prepared from a stock of tribromoethanol (1 g/ml) in 2-methyl-2-butanol, diluted 1:20 in saline, and dosed as 10 μl/g body weight. Hepatocytes were isolated by collagenase perfusion as previously described (*76*). Hepatocytes were seeded in medium Eagle-199 (MEM-199) containing penicillin G (100 U/ml), streptomycin (100 μg/ml), and 10% (v/v) FBS. Hepatocytes were left for attachment (3 to 4 hours) and cultured overnight at 37°C with 5% CO_2 in MEM-199 supplemented with penicillin G (100 U/ml), streptomycin (100 μg/ml), 10 nM insulin, and 100 nM dexamethasone.

Cell culture and treatments

Tig3 (provided by K. Helin), HeLa, HEK293T (from the American Type Culture Collection), and MEFs were cultured in DMEM supplemented with 10% FBS and penicillin/streptomycin (10,000 U/ml). Hepatocytes were cultured as described above. Hexa KO and WT HeLa cells were provided by M. Lazarou (*77*). All cell lines were maintained in a 5% CO_2 incubator at 37°C. The induction of autophagy by nutrient starvation was achieved by washing the cells with PBS and incubating with HBSS for the indicated time periods. Treatments with PP242 (500 nM) were used for indicated time points. BafA1 treatments were 2 to 4 hours as indicated (200 nM). For cycloheximide chase experiments, cells were treated with cycloheximide (100 μg/ml) for indicated time points. All cell lines were regularly tested and verified to be mycoplasma negative by sequencing.

Antibodies

Antibodies used in this study with dilutions used for Western blot are mentioned here. Mouse monoclonal anti–MYC-Tag (1:1000, 2276), rabbit monoclonal anti–HA-Tag (1:1000, 3724), rabbit monoclonal anti-ATG14 (1:1000, 96752), rabbit monoclonal anti–Ser^{29}-ATG14 (1:1000, 3979), rabbit polyclonal anti–Ser^{757}-ULK1 (1:500, 6888), rabbit monoclonal anti-rabbit polyclonal anti-p70 S6 kinase (1:1000, 9202), mouse monoclonal anti–Thr^{389}-p70 S6 kinase (1:1000, 9206), rabbit monoclonal anti-AMPKα (1:1000, 4150), rabbit monoclonal anti–Thr^{172}-AMPKα (1:1000, 4188), and rabbit monoclonal anti-ubiquitin (1:2000, 43124) were from Cell Signaling Technology. Rabbit polyclonal anti-LC3B was from Cell Signaling Technology (1:2000, 2775), and mouse monoclonal anti-LC3B was from Nanotools (1:2000, 0260-100/LC3-2G6). Rabbit monoclonal anti-ULK1 was from Cell Signaling Technology (1:1000, 8054). Rabbit polyclonal anti-ULK1 was from Proteintech (1:500, 20986-1-AP). Rabbit polyclonal anti-GABARAP (N term) (1:1000, AP1821a) was from Abgent. Rabit polyclonal anti-p62 (1:2000, PM045) and mouse monoclonal anti-monomeric Keima-Red (1:1000, M126-3 M) were from MBL International. Rabbit polyclonal anti–glyceraldehyde-3-phosphate dehydrogenase (GAPDH) (1:3000, 25778) and mouse monoclonal anti-GFP (1:2000, sc-9996) were from Santa Cruz Biotechnology. Mouse monoclonal anti-vinculin (1:5000, V9131) and mouse monoclonal anti-Flag M2 (1:1000, F1804) were from Sigma-Aldrich. Rat monoclonal anti-LAMP2 (ab13524) was from Abcam.

Reagents and inhibitors

LysoTracker Deep Red (L12492), Bodipy 493/503 (D3922), and PowerUp SYBR Green Master Mix (A25742) were obtained from Thermo Fisher Scientific (D3922). MYC-trap (ytma-100) and GFP-trap (gtma-100) beads were obtained from ChromeTek. Anti-Flag M2 magnetic beads (M8823-1ML) were from Sigma-Aldrich. HA magnetic beads were from Pierce (88836). Gateway BP Clonase II Enzyme mix (11789020), Gateway LR Clonase II Enzyme mix (11791020), Nile red (N1142), and Protein G magnetic beads (10004D) were from Invitrogen. QuikChange II XL Site-Directed Mutagenesis Kit (200521) was from Agilent Technologies. Blasticidin S (SBR00022) was from Santa Cruz Biotechnology. Doxycycline hyclate (D9891), mTOR Inhibitor III, PP242 (475988), HBSS (H8264), and Insulin (I9278) were from Sigma-Aldrich. Cycloheximide (C7698), Protease Inhibitor (P8340), OptiPrep Density Gradient Medium (D1556), and tribromoethanol (T48402) in 2-methyl-2-butanol (152463) were obtained from Sigma-Aldrich. Torin1 was from Selleck Chemicals (S2827). BafA1 was from Santa Cruz Biotechnology (sc-201550B). 26*S* proteasome inhibitor MG132 (tlrl-mg132) and NP-40 (FNN0021) were from Invitrogen. Enhanced chemiluminescence system (RPN2236) was from Amersham. M-MLV Reverse Transcriptase (M1705) was from Promega. Mounting medium (S3025), horseradish peroxidase (HRP)–labeled Polymer Anti-Rabbit (K4003), and liquid 3,3′-Diaminobenzidine (DAB) substrate (K3468) were from Dako. For cell culturing, FBS (10270106), penicillin/streptomycin (15140122), and Medium-199 (31150022) were from Gibco.

Plasmids, siRNA, and transfection

pRK5-HA-Ubiquitin-K48 (#17605), HA-Ubiquitin (#18712), pRK5-HA-Ubiquitin-K63 (#17606), HA-hULK1 (#31963), and Flag-TRAF6 (#21624) were from Addgene. All six human ATG8s were derived from N-terminal myc-AP2–tagged hATG8s shared by C. Behrends (Ludwig-Maximilians-Universität) (*78*) and were recloned into the pCDH-EF1-GFP backbone. All six GST-ATG8s constructs were gifts from T. Johansen (University of Tromsø), and the GST-GABARAP LDS mutant was provided by C. Behrends. The mKeima fluorophore was provided by A. Miyawaki (RIKEN Brain Science Institute, Japan). Using In-Fusion cloning (TaKaRa, 638943), mKeima was fused with RPL10A or LC3B for the assembly into the pLVX-TetOne–inducible lentiviral plasmid backbone (TaKaRa, 638144). RPL10A was amplified from a GFP-RPL10A plasmid provided by R. Agami (Netherlands Cancer Institute). PELI3 was amplified from Tig3 cDNA and integrated into the pLVX-TetOne-GFP backbone for inducible expression using NEBuilder HiFi DNA Assembly kit (NEB, E2621L). The Peli3 and ULK1 truncates were generated by gateway cloning. Gateway vectors were gifts from S. Geley (Innsbruck Medical University) (*79*). Point mutations were created by using a site-directed mutagenesis kit (200523; Agilent Technologies). Plasmid constructs were verified by conventional restriction enzyme digestion and/or by DNA sequencing. For screen validations, PELI3 siRNAs (4392420, 4392420), Control siRNA (4390844), and ULK1 siRNA (s15963) were purchased from Thermo Fisher Scientific. Transient transfections were performed with RNAiMAX (Invitrogen) or Lipofectamine 2000 (Invitrogen) according to the manufacturer's instructions. Regarding siRNA transfections for the screen, please see separate screen description.

Lentivirus and cell line production

HEK293T cells were transfected with the respective lentiviral expression plasmid together with envelope and packaging vectors, pCMV-VSVG and PAX8, using Lipofectamine 2000 (Thermo Fisher Scientific). After 24 hours, the supernatant containing virus was filtered through a 0.45-μm filter and mixed with polybrene (8 μg/ml) (Sigma-Aldrich, #107689) to infect target cells. Transduced cells were selected by antibiotic selection.

High-content screening procedure

The screening library primarily consisted of the predesigned Silencer Select human ubiquitin siRNA library (Thermo Fisher Scientific, A30140), which targets 981proteins. We updated the library by adding additional identified E2 and E3 enzymes, as well as deubiquitinating enzymes (*80*, *81*). The final library targeted 1192 genes listed in table S1. Each gene was targeted with three independent siRNAs. The plate design of the library (384-well) was chosen so that each of the three siRNAs targeting a gene were on different plates and at different positions of the plates to exclude plate and positional bias. Each plate was spotted with positive (siULK1, siBECN1) and negative (siControl) controls. Cells were reverse-transfected in a total volume of 50 μl of full medium supplemented with doxycycline (100 ng/ml). Twenty-four hours after transfection, 50 μl of new medium containing doxycycline was added. Forty-eight hours after transfection, cells were washed and starved for 24 hours in HBSS without doxycycline. All liquid handling was performed by the Microlab STARlet Liquid Handling robot (Hamilton). The primary as well as the validation screen were each performed in two independent biological replicates. Before imaging, cells were incubated with Hoechst 33342 (1.67 μg/ml) for 15 min. Imaging was performed by the ImageExpress microscope (Molecular Devices) at 37°C with 5% CO_2 using the 40× objective. Hoechst 33342 was imaged using the DAPI (4′,6-diamidino-2-phenylindole) filter set. Acid Keima was imaged using the Texas Red filter set with a digital confocal correction of 0.17. Nine images for 96-well plates (validation screen) and six images for 384-well plates (primary screen) were acquired per well. Image analysis was performed using MetaExpress software using a pipeline developed for identification and quantification of perinuclear puncta.

Screen data analysis

Data normalization

Following image acquisition and analysis, the obtained data were further analyzed using R. Data from single cells were averaged for each well to reduce noise, resulting in the quantification of average mKeima puncta per cell for each well. Each acquired plate was normalized and scaled independently as follows: Average mKeima puncta per cell were normalized by the median of the siControl wells. Next, to reduce effect variation of the positive controls between plates and between cell lines, the normalized average mKeima puncta per cell were scaled to the positive control (siULK1) for each plate following the function

$$f(x) = \exp\left[\frac{\ln(x)}{\ln(\mu_{\mathrm{ULK1}})} \times \ln(0.1)\right] \text{ for } x < 1$$

$$f(x) = x \text{ for } x > 1$$

This scaling function uses the median signal of the positive control siULK1 (μULK1) and sets it to 0.1 while keeping the siControl median at 1.0 and scaling all other siRNA effects relative to the positive and negative control, making the inhibition effect of siRNAs more comparable across plates and cell lines.

Primary screen scoring

RSA analysis was used to rank the effect of screened siRNAs from the primary screen (*30*). In brief, RSA analysis uses a cumulated hypergeometric distribution function to rank siRNAs by effect potency while also prioritizing genes with multiple hitting siRNAs. RSA analysis was performed using the "runRSA" function within the "staRank" package for both down- and up-regulation of lysosomal Keima puncta. Boundaries for down-regulation were set to 0.6 and 0.5. Boundaries for up-regulation were set to 1.4 and 1.5. The *P* values from the two repetitions of the screen were combined using Fisher's method. The mean effect of all siRNAs per gene, together with the combined *P* value, is summarized in table S1.

Validation screen scoring

The two strongest siRNAs for each significant hit from the primary screen were selected and further used in the validation screen. In the validation screen, selected siRNAs were tested in Tig3 cells expressing mKeima-RPL10A and mKeima-LC3B, respectively. The validation screen was performed, and the acquired data were normalized, as described above. The RSA algorithm assumes a large population of siRNAs with a normal distribution and a mean close to 1. Because of the reduced number of siRNAs and the induced bias toward functional siRNAs, the RSA analysis is not feasible to score functional gene targets in the validation screen. Thus, for each cell line, the mean of the two siRNAs per gene was tested against the mean of siControl using Dunnett's test. The *P* values were adjusted using the Benjamini-Hochberg method. Selection criteria included an adjusted *P* value of <0.01 and an

FC of <0.5 relative to siControl. The mean effect of all siRNAs per gene and their *P* values are summarized in table S2 for each cell line.

Protein lysate

The cell or tissue lysates were prepared in NP-40 or radioimmunoprecipitation assay (RIPA) buffer [20 mM tris (pH 8.0), 1 mM EDTA, 0.5 mM EGTA, 0.1% sodium deoxycholate, 150 mM NaCl, 1% IGEPAL (Sigma-Aldrich), 10% glycerol] supplemented with protease inhibitor cocktail and phosphatase inhibitors. Protein concentration was measured by DC protein assay kit (Bio-Rad). For insoluble fractions, the lysate pellets were dissolved in RIPA containing 2% SDS.

Co-IP assay

Co-IPs were performed as previously described (*82*). Briefly, cellular or tissue lysates were incubated with the indicated antibody at 4°C for 2 hours on a Rotospin rotary mixer followed by incubation with Protein G magnetic beads (Invitrogen, #10004D) for 2 hours at 4°C. Co-IPs for exogenously expressed proteins were performed by incubating the lysates with antibody-conjugated magnetic beads for 1 hour at 4°C. The beads were washed with 3× ice-cold PBS. The proteins were eluted from washed beads by boiling for 5 min in 2× SDS gel loading dye before immunoblot analysis.

Western blotting

Protein lysates were diluted in Laemmli buffer [4×, Invitrogen, 0.093 mg/ml dithiothreitol (DTT)] and boiled at 95°C for 5 min. Proteins were resolved on 4 to 15% Criterion TGX Stain-Free Protein Gels (Bio-Rad) and blotted to a polyvinylidene difluoride membrane by semidry transfer, using a Trans-Blot Turbo Transfer System (Bio-Rad). Next, the membranes were incubated in primary antibody overnight at 4°C, washed with 3× PBS/PBST followed by incubation with HRP-conjugated secondary antibody for 1 hour at room temperature. After washing with 3× PBS/PBST, the blots were developed using an enhanced chemiluminescence system. The signal was captured using a ChemiDoc MP System (Bio-Rad) provided with the Image Lab 6.0.1 Software (Bio-Rad). Densiometric quantifications of the immunoblots were analyzed with the Image Lab 6.1 software.

GST pull-down assay

GST pulldown assay was performed as previously described (*82*). GST or GST-ATG8 proteins were expressed in SoluBL21 (Amsbio), and the proteins were purified on Glutathione Sepharose 4 Fast-Flow beads (GE Healthcare). [^{35}S]-labeled MYC-PELI3 protein was in vitro translated using TnT T7–coupled reticulocyte lysate system (Promega). GST or GST-ATG8s were incubated with [^{35}S]-labeled MYC-PELI3 in 250 ml of NETN-E buffer [50 mM tris (pH 8.0), 100 mM NaCl, 6 mM EDTA, 6 mM EGTA, 0.5% NP-40, and 1 mM DTT supplemented with complete mini EDTA-free protease inhibitor cocktail (Roche)] for 2 hours at 4°C. Then, GST beads were added and the mixture was incubated for 30 min at room temperature. The beads were washed with NETN-E buffer five times, boiled with loading buffer, and subjected to SDS-PAGE (polyacrylamide gel electrophoresis). The gel was stained with Coomassie Blue and vacuum-dried. GST or GST-ATG8s was detected by staining with Coomassie Blue, whereas the [^{35}S]-labeled MYC-PELI3 was detected in PharosFX imager (Bio-Rad Laboratories).

Proteinase K protection assay

Proteinase K protection assay was performed according to Zhang *et al.* (*83*). HEK293T cells were treated as indicated, scraped in PBS, and centrifuged at 500*g*. The cells were then resuspended in 250 μl of lysis buffer containing 20 mM Hepes-KOH (pH 7.2), 1 mM EDTA, 400 mM sucrose, and 0.3 mM DTT. Next, cells were homogenized by passing through 22-gauge needle to achieve 90% cell lysis, tested by trypan blue exclusion. Samples were centrifuged at 1000*g* for 5 min at 4°C. Supernatants were collected, and the protein content was measured. Equal amounts of proteins were treated with proteinase K (10 mg/ml) with or without 0.5% Triton X-100 on ice for 20 min. Reaction was stopped by addition of protease inhibitor, and the samples were boiled in 4× SDS sample buffer followed by Western blot analysis.

Immunofluorescence confocal microscopy

For immunofluorescence, cells cultured on coverslips were washed with PBS and fixed in 4% paraformaldehyde for 10 min. Next, cells were permeabilized with 0.1% Triton X-100 for 10 min, followed by blocking with 1% bovine serum albumin (BSA) for 30 min at room temperature. Further, cells were incubated with primary antibody overnight at 4°C and washed thrice with PBS followed by 1-hour incubation with Alexa Flour–conjugated secondary antibody. Cells were counterstained with Hoechst 33342. Cells were washed thrice with PBS, mounted using antifade mounting medium (Dako), and air-dried. For neutral lipids, cells were stained using with Bodipy 493/503 (10 μg/ml) for 20 min at room temperature. Images were acquired on LSM 800 (oil objective ~63 Å/1.4; Carl Zeiss) confocal microscopes, and the representative images were prepared using ImageJ Fiji. Colocalization analysis was performed using Zen software (Zeiss). Puncta quantification was performed using Cell Profiler software. Here, cells were segmented based on nuclear stain and expanded to the size of the cytoplasm to approximate the whole cell and a number of puncta were counted and plotted for each individual cell. For BODIPY and Lamp2 proximity analysis, puncta were segmented and nearest-neighbor analysis used to count the number of Lamp2-positive objects immediately adjacent/in 5-pixel proximity to each BODIPY object. For puncta quantifications related to the high-content screen, see separate screen description.

Immunohistochemistry

Freshly isolated mouse tissues were fixed in 4% paraformaldehyde for 2 days. For paraffin embedding, tissues were dehydrated in increasing alcohol concentrations, followed by xylene and finally in paraffin using the automatic spin tissue processor (Thermo Fisher Scientific, #STP120). Paraffin-embedded tissues were sectioned at a thickness of 5 μm. The sections were deparaffinized in xylene, rehydrated with a gradient (100% to 70%) of ethanol, and washed in distilled water. Sections were stained with hematoxylin and eosin (H&E) stain (Sigma-Aldrich, GHS116 and HT110116). For antibody staining, endogenous peroxidase activity was blocked at room temperature by H_2O_2. Antigen retrieval was performed in a steam microwave with sodium citrate buffer (pH 6.0) for 10 min followed by permeabilization with PBS (pH 7.4) containing 0.25% Triton X-100, blocked in FBS, and incubated overnight with indicated antibodies. The next day, the sections were washed twice with PBS (pH 7.4) containing 0.1% Triton X-100, followed by incubation with either Alexa Fluor–conjugated immunoglobulin G (IgG) or HRP-conjugated anti-rabbit IgG. Sections were washed and developed

with DAB peroxidase substrate kit. Sections were finally counterstained with hematoxylin stain (VectorLabs, #H-3502) followed by dehydration through an alcohol gradient and mounted with permanent mounting medium (Dako). The slides were visualized under a Leica ICC50 microscope. For cryosectioning, freshly harvested tissues were fixed in 4% paraformaldehyde overnight followed by 30% sucrose. Next, tissues were frozen in Tissue-Tek optimum cutting temperature compound (OCT) and sectioned at a thickness of 10 μm using cryostat (Leica).

Transmission electron microscopy

Cells were seeded on Thermanox coverslips to reach 80% confluency. The next day, cells were starved in HBSS in the presence of 200 nM BafA1 for 2 hours. Cells were washed with PBS and fixed with 2% (v/v) glutaraldehyde in 0.05 M sodium phosphate buffer (pH 7.2) for 24 hours. Subsequently, specimens were processed for TEM as described previously (*84*, *85*). For tissues, mice were perfused with 2% (v/v) glutaraldehyde in 0.05 M sodium phosphate buffer (pH 7.2), followed by incubation in 2% glutaraldehyde for 24 hours before processing the samples for TEM. All TEM imaging was performed on a CM-100 transmission electron microscope (Philips). Autophagic vesicles per cross section were quantified by applying the following criteria: Vesicles with double/multiple membranes ranging between 0.3 and 0.7 μm, luminal density similar to cytosol/containing organelles or partial organelles, were considered as autophagic vesicles. Quantification of LD contacts with or engulfment by autophagic/lysosomal membranes or vesicles was performed using classification as described previously (*86*). Quantifications were performed per 1-μm^2 area.

RNA isolation and quantitative real-time PCR

RNA isolation and qRT-PCR were performed as previously described (*85*). Briefly, total RNA was extracted using TRIzol reagent according to the manufacturer's protocols (Invitrogen). RNA (1 μg) was used for reverse transcription using an M-MLV reverse transcriptase, and qRT-PCR was performed using Power SYBR Green PCR master mix. The FC in expression was calculated by the $2^{-\Delta\Delta Ct}$ method. mRNA expression profiles were normalized to levels of housekeeping genes GAPDH or HPRT in each sample. The primers used in qRT-PCR are listed below.

Human GAPDH-FAACGGATTTGGTCGTATTGG
Human GAPDH-RCTTCCCGTTCTCAGCCTT
Human PELI3-F1ACTTGCTGATAGCCACTATGGG
Human PELI3-R1TGAAGCCGTGTTGCCATTTG
Human PELI3-F2ATCTCGGTCTGTGGGAATGTG
Human PELI3-R2AGCACGTTGGACTCGTTTTC
Mouse HPRT TCAGTCAACGGGGGACATAAA
Mouse HPRT TCCAACACTTCGAGAGGTCC
Mouse PELI3 GAGAGCCCCAGAACGCCG
Mouse PELI3 TAGAGCGGCCAATCTGGAACA

Membrane fractionation

Membrane fractionation was performed as previously described (*42*, *43*). Briefly, Tig3 cells expressing GFP or GFP-PELI3 cells were plated in 15-cm^2 dishes (two dishes per sample). The next day, cells were starved for 2 hours in HBSS in the presence of BafA1. For the sequential centrifugation, cells were harvested, and the cell pellet was resuspended in B1 buffer containing 20 mM Hepes-KOH (pH 7.2), 400 mM sucrose, and 1 mM EDTA, protease inhibitors, and 0.3 mM DTT. Resuspended cell pellet was passed through 22-gauge needle to achieve 90% lysis. Homogenates were subjected to sequential centrifugation at 3000*g* for 10 min, and the supernatant was collected and centrifuged at 25,000*g* for 20 min. Next, the supernatant from the 25,000*g* fraction was centrifuged at 100,000*g* for 30 min. Inputs from each step of centrifugation were collected. Pellets were dissolved in 2× Laemmli buffer, boiled for 5 min, and analyzed by Western blotting. For OptiPrep membrane floating assays, B1 buffer homogenates were centrifuged at 3000*g* for 10 min and the supernatant was mixed with equal volume of OptiPrep. Discontinuous gradients were prepared in SW41 tubes (Beckman Instruments) by overlaying 2.4 ml of diluted supernatant in 30% OptiPrep, 2.4 ml of 25% OptiPrep, 2 ml of 15%, 2 ml of 10%, 0.5 ml of 0.5%, and 0.5 ml of 0%. The gradients were centrifuged at 150,000*g* for 2 hours, and subsequently, 11 fractions (0.85 ml) were collected. Fractions were diluted in equal volume of homogenization buffer, and membranes were enriched by centrifugation at 100,000*g* for 40 min. The pellets were dissolved in 2× Laemmli buffer and analyzed by Western blotting.

Quantification and statistical analysis

All data are expressed as mean ± SD or mean ± SEM. Statistical analysis was performed using GraphPad Prism 10. Unless otherwise stated, comparisons of two groups used a two-t ailed unpaired Student's *t* test. For experiments in which more than two groups were compared, ordinary one-way analysis of variance (ANOVA) was performed followed by the Brown-Forsythe and Bartlett's test. *P* value of 0.05 or less was deemed statistically significant in all of these statistical tests. Statistical details and results of experiments are described in the relevant figures and figure legends.

Shotgun lipidomics

Shotgun lipidomics analysis was performed as described previously (*87*) to determine the TAG and CE contents of liver homogenates. In brief, 20 μl of liver homogenate was diluted with 180 μl of 155 mM ammonium bicarbonate and spiked with a series of internal lipid standards. Lipids were extracted using a modified Bligh and Dyer protocol (*88*) by the addition of 1 ml of chloroform/methanol 2:1 (v/v) and infused into the Orbitrap Fusion Tribrid mass spectrometer (Thermo Fisher Scientific, San Jose, CA, United States) using a robotic system of TriVersa NanoMate (Advion Biosciences, Ithaca, NY, USA). Mass spectra were acquired in both the positive and negative ionization modes and processed with the Python-based software LipidXplorer (*89*) to identify lipid species fulfilling a set of criteria defined in the molecular fragmentation query language (MFQL) files (*90*). Ion intensities of identified lipid species and spiked internal standards reported by LipidXplorer were used to determine the absolute quantities of species in the TAG and glycerophospholipid (GPL) classes (phosphatidylcholine, phosphatidylethanolamine, phosphatidylserine, phosphatidylinositol, phosphatidylglycerol, phosphatidic acid, cardiolipin, and their ether and lyso variants) with LipidQ, an in-house built R-based software (https://github.com/ELELAB/lipidQ). The total molar quantities of TAGs, CEs, and GPLs were calculated and used to determine the relevant ratios.

PELI3 and autophagy gene set expression analysis from control and MASLD patients

Gene expression data from 23 individuals with normal weight and 44 individuals with MASLD were obtained from GSE126848 (*55*) and Lewinska *et al.* (*56*). Fastq files were trimmed with Trimmomatic-0-2.36 (TruSeq3-PE illumina adapters cut). Reads were annotated

with STAR-2.5.1a to hg38 canonical genome assembly 1 pass mode, with default parameters. Gene reference (Gencode.v30) was used for gene abundancy estimation and normalized by gene length [transcript per million (TPM)]. ssGSEA was used to associate curated lists of autophagy genes (table S3) with the Lewinska *et al.* (*56*) dataset using GenePattern 2.0 (*91*). Enrichment scores between the groups were compared using nonparametric Kruskal-Wallis test and plotted using GraphPad Prism 10.1.0. Only samples expressing all autophagy genes were included in the analysis.

Supplementary Materials

The PDF file includes:
Figs. S1 to S6
Legends for tables S1 to S3
Uncropped blots

Other Supplementary Material for this manuscript includes the following:
Tables S1 to S3

REFERENCES AND NOTES

1. A. Efeyan, W. C. Comb, D. M. Sabatini, Nutrient-sensing mechanisms and pathways. *Nature* **517**, 302–310 (2015).
2. Y. Sung, Y. C. Yu, J. M. Han, Nutrient sensors and their crosstalk. *Exp. Mol. Med.* **55**, 1076–1089 (2023).
3. A. Kuma, M. Hatano, M. Matsui, A. Yamamoto, H. Nakaya, T. Yoshimori, Y. Ohsumi, T. Tokuhisa, N. Mizushima, The role of autophagy during the early neonatal starvation period. *Nature* **432**, 1032–1036 (2004).
4. P. Ylä-Anttila, H. Vihinen, E. Jokitalo, E.-L. Eskelinen, Monitoring autophagy by electron microscopy in mammalian cells. *Methods Enzymol.* **452**, 143–164 (2009).
5. L. Yu, Y. Chen, S. A. Tooze, Autophagy pathway: Cellular and molecular mechanisms. *Autophagy* **14**, 207–215 (2018).
6. D. J. Klionsky, G. Petroni, R. K. Amaravadi, E. H. Baehrecke, A. Ballabio, P. Boya, J. M. B.-S. Pedro, K. Cadwell, F. Cecconi, A. M. K. Choi, M. E. Choi, C. T. Chu, P. Codogno, M. I. Colombo, A. M. Cuervo, V. Deretic, I. Dikic, Z. Elazar, E.-L. Eskelinen, G. M. Fimia, D. A. Gewirtz, D. R. Green, M. Hansen, M. Jäättelä, T. Johansen, G. Juhász, V. Karantza, C. Kraft, G. Kroemer, N. T. Ktistakis, S. Kumar, C. Lopez-Otin, K. F. Macleod, F. Madeo, J. Martinez, A. Meléndez, N. Mizushima, C. Münz, J. M. Penninger, R. M. Perera, M. Piacentini, F. Reggiori, D. C. Rubinsztein, K. M. Ryan, J. Sadoshima, L. Santambrogio, L. Scorrano, H.-U. Simon, A. K. Simon, A. Simonsen, A. Stolz, N. Tavernarakis, S. A. Tooze, T. Yoshimori, J. Yuan, Z. Yue, Q. Zhong, L. Galluzzi, F. Pietrocola, Autophagy in major human diseases. *EMBO J.* **40**, e108863 (2021).
7. N. Martinez-Lopez, R. Singh, Autophagy and lipid droplets in the liver. *Annu. Rev. Nutr.* **35**, 215–237 (2015).
8. R. Singh, S. Kaushik, Y. Wang, Y. Xiang, I. Novak, M. Komatsu, K. Tanaka, A. M. Cuervo, M. J. Czaja, Autophagy regulates lipid metabolism. *Nature* **458**, 1131–1135 (2009).
9. Y. Minami, A. Hoshino, Y. Higuchi, M. Hamaguchi, Y. Kaneko, Y. Kirita, S. Taminishi, T. Nishiji, A. Taruno, M. Fukui, Z. Arany, S. Matoba, Liver lipophagy ameliorates nonalcoholic steatohepatitis through extracellular lipid secretion. *Nat. Commun.* **14**, 4084 (2023).
10. N. Hosokawa, T. Sasaki, S. Iemura, T. Natsume, T. Hara, N. Mizushima, Atg101, a novel mammalian autophagy protein interacting with Atg13. *Autophagy* **5**, 973–979 (2009).
11. N. Hosokawa, T. Hara, T. Kaizuka, C. Kishi, A. Takamura, Y. Miura, S. Iemura, T. Natsume, K. Takehana, N. Yamada, J.-L. Guan, N. Oshiro, N. Mizushima, Nutrient-dependent mTORC1 association with the ULK1-Atg13-FIP200 complex required for autophagy. *Mol. Biol. Cell* **20**, 1981–1991 (2009).
12. I. G. Ganley, D. H. Lam, J. Wang, X. Ding, S. Chen, X. Jiang, ULK1.ATG13.FIP200 complex mediates mTOR signaling and is essential for autophagy. *J. Biol. Chem.* **284**, 12297–12305 (2009).
13. R. C. Russell, Y. Tian, H. Yuan, H. W. Park, Y.-Y. Chang, J. Kim, H. Kim, T. P. Neufeld, A. Dillin, K.-L. Guan, *ULK1* induces autophagy by phosphorylating Beclin-1 and activating VPS34 lipid kinase. *Nat. Cell Biol.* **15**, 741–750 (2013).
14. T. Proikas-Cezanne, Z. Takacs, P. Dönnes, O. Kohlbacher, WIPI proteins: Essential PtdIns3P effectors at the nascent autophagosome. *J. Cell Sci.* **128**, 207–217 (2015).
15. F. O. Farrell, T. E. Rusten, H. Stenmark, Phosphoinositide 3-kinases as accelerators and brakes of autophagy. *FEBS J.* **280**, 6322–6337 (2013).
16. H. Weidberg, E. Shvets, T. Shpilka, F. Shimron, V. Shinder, Z. Elazar, LC3 and GATE-16/GABARAP subfamilies are both essential yet act differently in autophagosome biogenesis. *EMBO J.* **29**, 1792–1802 (2010).
17. H. Weidberg, T. Shpilka, E. Shvets, A. Abada, F. Shimron, Z. Elazar, LC3 and GATE-16 N termini mediate membrane fusion processes required for autophagosome biogenesis. *Dev. Cell* **20**, 444–454 (2011).
18. M. Antonioli, F. Albiero, F. Nazio, T. Vescovo, A. B. Perdomo, M. Corazzari, C. Marsella, P. Piselli, C. Gretzmeier, J. Dengjel, F. Cecconi, M. Piacentini, G. M. Fimia, AMBRA1 interplay with cullin E3 ubiquitin ligases regulates autophagy dynamics. *Dev. Cell* **31**, 734–746 (2014).
19. R.-H. Chen, Y.-H. Chen, T.-Y. Huang, Ubiquitin-mediated regulation of autophagy. *J. Biomed. Sci.* **26**, 80 (2019).
20. P. Grumati, I. Dikic, Ubiquitin signaling and autophagy. *J. Biol. Chem.* **293**, 5404–5413 (2018).
21. C.-C. Liu, Y.-C. Lin, Y.-H. Chen, C.-M. Chen, L.-Y. Pang, H.-A. Chen, P.-R. Wu, M.-Y. Lin, S.-T. Jiang, T.-F. Tsai, R.-H. Chen, Cul3-KLHL20 ubiquitin ligase governs the turnover of ULK1 and VPS34 complexes to control autophagy termination. *Mol. Cell* **61**, 84–97 (2016).
22. F. Nazio, M. Carinci, C. Valacca, P. Bielli, F. Strappazzon, M. Antonioli, F. Ciccosanti, C. Rodolfo, S. Campello, G. M. Fimia, C. Sette, P. Bonaldo, F. Cecconi, Fine-tuning of ULK1 mRNA and protein levels is required for autophagy oscillation. *J. Cell Biol.* **215**, 841–856 (2016).
23. W. Wan, Z. You, L. Zhou, Y. Xu, C. Peng, T. Zhou, C. Yi, Y. Shi, W. Liu, mTORC1-regulated and HUWE1-Mediated WIPI2 degradation controls autophagy flux. *Mol. Cell* **72**, 303–315.e6 (2018).
24. A. Scrivo, P. Codogno, P. Bomont, Gigaxonin E3 ligase governs ATG16L1 turnover to control autophagosome production. *Nat. Commun.* **10**, 780 (2019).
25. S. Yang, B. Wang, F. Humphries, R. Jackson, M. E. Healy, R. Bergin, G. Aviello, B. Hall, D. McNamara, T. Darby, A. Quinlan, F. Shanahan, S. Melgar, P. G. Fallon, P. N. Moynagh, Pellino3 ubiquitinates RIP2 and mediates Nod2-induced signaling and protective effects in colitis. *Nat. Immunol.* **14**, 927–936 (2013).
26. S. Yang, B. Wang, L. S. Tang, J. Siednienko, J. J. Callanan, P. N. Moynagh, Pellino3 targets RIP1 and regulates the pro-apoptotic effects of TNF-α. *Nat. Commun.* **4**, 2583 (2013).
27. Y.-M. Kim, H.-Y. Kim, H. T. Ha Thi, J. Kim, Y. J. Lee, S.-J. Kim, S. Hong, Pellino 3 promotes the colitis-associated colorectal cancer through suppression of IRF4-mediated negative regulation of TLR4 signalling. *Mol. Oncol.* **17**, 2380–2395 (2023).
28. A. R. Kristensen, S. Schandorff, M. Høyer-Hansen, M. O. Nielsen, M. Jäättelä, J. Dengjel, J. S. Andersen, Ordered organelle degradation during starvation-induced autophagy. *Mol. Cell. Proteomics* **7**, 2419–2428 (2008).
29. H. Katayama, T. Kogure, N. Mizushima, T. Yoshimori, A. Miyawaki, A sensitive and quantitative technique for detecting autophagic events based on lysosomal delivery. *Chem. Biol.* **18**, 1042–1052 (2011).
30. R. König, C. Chiang, B. P. Tu, S. F. Yan, P. D. DeJesus, A. Romero, T. Bergauer, A. Orth, U. Krueger, Y. Zhou, S. K. Chanda, A probability-based approach for the analysis of large-scale RNAi screens. *Nat. Methods* **4**, 847–849 (2007).
31. H. Li, C. Li, W. Zhai, X. Zhang, L. Li, B. Wu, B. Yu, P. Zhang, J. Li, C.-P. Cui, L. Zhang, Destabilization of TP53 by USP10 is essential for neonatal autophagy and survival. *Cell Rep.* **41**, 111435 (2022).
32. Y. Chu, Y. Kang, C. Yan, C. Yang, T. Zhang, H. Huo, Y. Liu, LUBAC and OTULIN regulate autophagy initiation and maturation by mediating the linear ubiquitination and the stabilization of ATG13. *Autophagy* **17**, 1684–1699 (2021).
33. S. Tian, S. Jin, Y. Wu, T. Liu, M. Luo, J. Ou, W. Xie, J. Cui, High-throughput screening of functional deubiquitinating enzymes in autophagy. *Autophagy* **17**, 1367–1378 (2021).
34. J. Zhang, V. Lachance, A. Schaffner, X. Li, A. Fedick, L. E. Kaye, J. Liao, J. Rosenfeld, N. Yachelevich, M.-L. Chu, W. G. Mitchell, R. G. Boles, E. Moran, M. Tokita, E. Gorman, K. Bagley, W. Zhang, F. Xia, M. Leduc, Y. Yang, C. Eng, L.-J. Wong, R. Schiffmann, G. A. Diaz, R. Kornreich, R. Thummel, M. Wasserstein, Z. Yue, L. Edelmann, A founder mutation in VPS11 causes an autosomal recessive leukoencephalopathy linked to autophagic defects. *PLOS Genet.* **12**, e1005848 (2016).
35. M. Komatsu, S. Waguri, T. Ueno, J. Iwata, S. Murata, I. Tanida, J. Ezaki, N. Mizushima, Y. Ohsumi, Y. Uchiyama, E. Kominami, K. Tanaka, T. Chiba, Impairment of starvation-induced and constitutive autophagy in Atg7-deficient mice. *J. Cell Biol.* **169**, 425–434 (2005).
36. D. Ma, M. M. Molusky, J. Song, C.-R. Hu, F. Fang, C. Rui, A. V. Mathew, S. Pennathur, F. Liu, J.-X. Cheng, J.-L. Guan, J. D. Lin, Autophagy deficiency by hepatic FIP200 deletion uncouples steatosis from liver injury in NAFLD. *Mol. Endocrinol.* **27**, 1643–1654 (2013).
37. J. Lee, J. Ha, J.-H. Kim, D. Seo, M. Kim, Y. Lee, S. S. Park, D. Choi, J. S. Park, Y. J. Lee, S. Yang, K.-M. Yang, S. M. Jung, S. Hong, S.-H. Koo, Y.-S. Bae, S.-J. Kim, S. H. Park, Peli3 ablation ameliorates acetaminophen-induced liver injury through inhibition of GSK3β phosphorylation and mitochondrial translocation. *Exp. Mol. Med.* **55**, 1218–1231 (2023).
38. S. Yang, B. Wang, F. Humphries, A. E. Hogan, D. O'Shea, P. N. Moynagh, The E3 ubiquitin ligase Pellino3 protects against obesity-induced inflammation and insulin resistance. *Immunity* **41**, 973–987 (2014).
39. J. Ezaki, N. Matsumoto, M. Takeda-Ezaki, M. Komatsu, K. Takahashi, Y. Hiraoka, H. Taka, T. Fujimura, K. Takehana, M. Yoshida, J. Iwata, I. Tanida, N. Furuya, D.-M. Zheng, N. Tada,

K. Tanaka, E. Kominami, T. Ueno, Liver autophagy contributes to the maintenance of blood glucose and amino acid levels. *Autophagy* **7**, 727–736 (2011).
40. A. Takagi, S. Kume, M. Kondo, J. Nakazawa, M. Chin-Kanasaki, H. Araki, S. Araki, D. Koya, M. Haneda, T. Chano, T. Matsusaka, K. Nagao, Y. Adachi, L. Chan, H. Maegawa, T. Uzu, Mammalian autophagy is essential for hepatic and renal ketogenesis during starvation. *Sci. Rep.* **6**, 18944 (2016).
41. I. Dikic, Z. Elazar, Mechanism and medical implications of mammalian autophagy. *Nat. Rev. Mol. Cell Biol.* **19**, 349–364 (2018).
42. S. Kumar, A. Jain, F. Farzam, J. Jia, Y. Gu, S. W. Choi, M. H. Mudd, A. Claude-Taupin, M. J. Wester, K. A. Lidke, T.-E. Rusten, V. Deretic, Mechanism of Stx17 recruitment to autophagosomes via IRGM and mammalian Atg8 proteins. *J. Cell Biol.* **217**, 997–1013 (2018).
43. T. Nishimura, N. Tamura, N. Kono, Y. Shimanaka, H. Arai, H. Yamamoto, N. Mizushima, Autophagosome formation is initiated at phosphatidylinositol synthase-enriched ER subdomains. *EMBO J.* **36**, 1719–1735 (2017).
44. S. Zellner, M. Schifferer, C. Behrends, Systematically defining selective autophagy receptor-specific cargo using autophagosome content profiling. *Mol. Cell* **81**, 1337–1354.e8 (2021).
45. E. Turco, M. Witt, C. Abert, T. Bock-Bierbaum, M.-Y. Su, R. Trapannone, M. Sztacho, A. Danieli, X. Shi, G. Zaffagnini, A. Gamper, M. Schuschnig, D. Fracchiolla, D. Bernklau, J. Romanov, M. Hartl, J. H. Hurley, O. Daumke, S. Martens, FIP200 claw domain binding to p62 Promotes autophagosome formation at ubiquitin condensates. *Mol. Cell* **74**, 330–346.e11 (2019).
46. C.-C. Lin, Y.-S. Huoh, K. R. Schmitz, L. E. Jensen, K. M. Ferguson, Pellino proteins contain a cryptic FHA domain that mediates interaction with phosphorylated IRAK1. *Structure* **16**, 1806–1816 (2008).
47. I. Kalvari, S. Tsompanis, N. C. Mulakkal, R. Osgood, T. Johansen, I. P. Nezis, V. J. Promponas, iLIR: A web resource for prediction of Atg8-family interacting proteins. *Autophagy* **10**, 913–925 (2014).
48. Y. Mei, M. Su, G. Soni, S. Salem, C. L. Colbert, S. C. Sinha, Intrinsically disordered regions in autophagy proteins. *Proteins* **82**, 565–578 (2014).
49. P.-M. Wong, C. Puente, I. G. Ganley, X. Jiang, The ULK1 complex: Sensing nutrient signals for autophagy activation. *Autophagy* **9**, 124–137 (2013).
50. E. Y. W. Chan, S. Kir, S. A. Tooze, siRNA screening of the kinome identifies ULK1 as a multidomain modulator of autophagy. *J. Biol. Chem.* **282**, 25464–25474 (2007).
51. J. Kim, M. Kundu, B. Viollet, K.-L. Guan, AMPK and mTOR regulate autophagy through direct phosphorylation of Ulk1. *Nat. Cell Biol.* **13**, 132–141 (2011).
52. M. Wirth, W. Zhang, M. Razi, L. Nyoni, D. Joshi, N. O'Reilly, T. Johansen, S. A. Tooze, S. Mouilleron, Molecular determinants regulating selective binding of autophagy adapters and receptors to ATG8 proteins. *Nat. Commun.* **10**, 2055 (2019).
53. G. Onal, O. Kutlu, D. Gozuacik, S. Dokmeci Emre, Lipid droplets in health and disease. *Lipids Health Dis.* **16**, 128 (2017).
54. Z. Li, R. J. Schulze, S. G. Weller, E. W. Krueger, M. B. Schott, X. Zhang, C. A. Casey, J. Liu, J. Stöckli, D. E. James, M. A. McNiven, A novel Rab10-EHBP1-EHD2 complex essential for the autophagic engulfment of lipid droplets. *Sci. Adv.* **2**, e1601470 (2016).
55. M. P. Suppli, K. T. G. Rigbolt, S. S. Veidal, S. Heebøll, P. L. Eriksen, M. Demant, J. I. Bagger, J. C. Nielsen, D. Oró, S. W. Thrane, A. Lund, C. Strandberg, M. J. Kønig, T. Vilsbøll, N. Vrang, K. L. Thomsen, H. Grønbæk, J. Jelsing, H. H. Hansen, F. K. Knop, Hepatic transcriptome signatures in patients with varying degrees of nonalcoholic fatty liver disease compared with healthy normal-weight individuals. *Am. J. Physiol. Gastrointest. Liver Physiol.* **316**, G462–G472 (2019).
56. M. Lewinska, A. Santos-Laso, E. Arretxe, C. Alonso, E. Zhuravleva, R. Jimenez-Agüero, E. Eizaguirre, M. J. Pareja, M. Romero-Gómez, M. Arrese, M. P. Suppli, F. K. Knop, S. K. Oversoe, G. E. Villadsen, T. Decaens, F. J. Carrilho, C. P. de Oliveira, B. Sangro, R. I. R. Macias, J. M. Banales, J. B. Andersen, The altered serum lipidome and its diagnostic potential for non-alcoholic fatty liver (NAFL)-associated hepatocellular carcinoma. *EBioMedicine* **73**, 103661 (2021).
57. N. Fujita, T. Itoh, H. Omori, M. Fukuda, T. Noda, T. Yoshimori, The Atg16L complex specifies the site of LC3 lipidation for membrane biogenesis in autophagy. *Mol. Biol. Cell* **19**, 2092–2100 (2008).
58. E. A. Alemu, T. Lamark, K. M. Torgersen, A. B. Birgisdottir, K. B. Larsen, A. Jain, H. Olsvik, A. Øvervatn, V. Kirkin, T. Johansen, ATG8 family proteins act as scaffolds for assembly of the ULK complex: Sequence requirements for LC3-interacting region (LIR) motifs. *J. Biol. Chem.* **287**, 39275–39290 (2012).
59. L. Zhang, C.-J. Ko, Y. Li, Z. Jie, L. Zhu, X. Zhou, X. Xie, T. Gao, T. Liu, X. Cheng, S.-C. Sun, Peli1 facilitates NLRP3 inflammasome activation by mediating ASC ubiquitination. *Cell Rep.* **37**, 109904 (2021).
60. F. Humphries, R. Bergin, R. Jackson, N. Delagic, B. Wang, S. Yang, A. V. Dubois, R. J. Ingram, P. N. Moynagh, The E3 ubiquitin ligase Pellino2 mediates priming of the NLRP3 inflammasome. *Nat. Commun.* **9**, 1560 (2018).
61. A. K. Giegerich, L. Kuchler, L. K. Sha, T. Knape, H. Heide, I. Wittig, C. Behrends, B. Brüne, A. von Knethen, Autophagy-dependent PELI3 degradation inhibits proinflammatory IL1B expression. *Autophagy* **10**, 1937–1952 (2014).
62. D. Gatica, V. Lahiri, D. J. Klionsky, Cargo recognition and degradation by selective autophagy. *Nat. Cell Biol.* **20**, 233–242 (2018).
63. A. L. Anding, E. H. Baehrecke, Cleaning house: Selective autophagy of organelles. *Dev. Cell* **41**, 10–22 (2017).
64. T. Lamark, T. Johansen, Mechanisms of selective autophagy. *Annu. Rev. Cell Dev. Biol.* **37**, 143–169 (2021).
65. T. B. Nguyen, S. M. Louie, J. R. Daniele, Q. Tran, A. Dillin, R. Zoncu, D. K. Nomura, J. A. Olzmann, DGAT1-dependent lipid droplet biogenesis protects mitochondrial function during starvation-induced autophagy. *Dev. Cell* **42**, 9–21.e5 (2017).
66. M. B. Schott, S. G. Weller, R. J. Schulze, E. W. Krueger, K. Drizyte-Miller, C. A. Casey, M. A. McNiven, Lipid droplet size directs lipolysis and lipophagy catabolism in hepatocytes. *J. Cell Biol.* **218**, 3320–3335 (2019).
67. T. T. P. Nguyen, D.-Y. Kim, Y.-G. Lee, Y.-S. Lee, X. T. Truong, J.-H. Lee, D.-K. Song, T. K. Kwon, S.-H. Park, C. H. Jung, C. Moon, T. F. Osborne, S.-S. Im, T.-I. Jeon, SREBP-1c impairs ULK1 sulfhydration-mediated autophagic flux to promote hepatic steatosis in high-fat-diet-fed mice. *Mol. Cell* **81**, 3820–3832.e7 (2021).
68. X. Xiong, R. Tao, R. A. DePinho, X. C. Dong, The autophagy-related gene 14 (Atg14) is regulated by forkhead box O transcription factors and circadian rhythms and plays a critical role in hepatic autophagy and lipid metabolism. *J. Biol. Chem.* **287**, 39107–39114 (2012).
69. C. Settembre, R. De Cegli, G. Mansueto, P. K. Saha, F. Vetrini, O. Visvikis, T. Huynh, A. Carissimo, D. Palmer, T. J. Klisch, A. C. Wollenberg, D. Di Bernardo, L. Chan, J. E. Irazoqui, A. Ballabio, TFEB controls cellular lipid metabolism through a starvation-induced autoregulatory loop. *Nat. Cell Biol.* **15**, 647–658 (2013).
70. S.-S. Takahashi, Y.-S. Sou, T. Saito, A. Kuma, T. Yabe, Y. Sugiura, H.-C. Lee, M. Suematsu, T. Yokomizo, M. Koike, S. Terai, N. Mizushima, S. Waguri, M. Komatsu, Loss of autophagy impairs physiological steatosis by accumulation of NCoR1. *Life Sci. Alliance* **3**, e201900513 (2020).
71. J. M. Kneeman, J. Misdraji, K. E. Corey, Secondary causes of nonalcoholic fatty liver disease. *Therap. Adv. Gastroenterol.* **5**, 199–207 (2012).
72. C.-W. Lin, H. Zhang, M. Li, X. Xiong, X. Chen, X. Chen, X. C. Dong, X.-M. Yin, Pharmacological promotion of autophagy alleviates steatosis and injury in alcoholic and non-alcoholic fatty liver conditions in mice. *J. Hepatol.* **58**, 993–999 (2013).
73. V. de Miranda Ramos, A. J. Kowaltowski, P. A. Kakimoto, Autophagy in Hepatic steatosis: A structured review. *Front. Cell Dev. Biol.* **9**, 657389 (2021).
74. A. Bradley, K. Anastassiadis, A. Ayadi, J. F. Battey, C. Bell, M.-C. Birling, J. Bottomley, S. D. Brown, A. Bürger, C. J. Bult, W. Bushell, F. S. Collins, C. Desaintes, B. Doe, A. Economides, J. T. Eppig, R. H. Finnell, C. Fletcher, M. Fray, D. Frendewey, R. H. Friedel, F. G. Grosveld, J. Hansen, Y. Hérault, G. Hicks, A. Hörlein, R. Houghton, M. H. de Angelis, D. Huylebroeck, V. Iyer, P. J. de Jong, J. A. Kadin, C. Kaloff, K. Kennedy, M. Koutsourakis, K. C. K. Lloyd, S. Marschall, J. Mason, C. McKerlie, M. P. McLeod, H. von Melchner, M. Moore, A. O. Mujica, A. Nagy, M. Nefedov, L. M. Nutter, G. Pavlovic, J. L. Peterson, J. Pollock, R. Ramirez-Solis, D. E. Rancourt, M. Raspa, J. E. Remacle, M. Ringwald, B. Rosen, N. Rosenthal, J. Rossant, P. R. Noppinger, E. Ryder, J. Z. Schick, F. Schnütgen, P. Schofield, C. Seisenberger, M. Selloum, E. M. Simpson, W. C. Skarnes, D. Smedley, W. L. Stanford, A. F. Stewart, K. Stone, K. Swan, H. Tadepally, L. Teboul, G. P. Tocchini-Valentini, D. Valenzuela, A. P. West, K. Yamamura, Y. Yoshinaga, W. Wurst, The mammalian gene function resource: The international knockout mouse consortium. *Mamm. Genome* **23**, 580–586 (2012).
75. M. E. Durkin, X. Qian, N. C. Popescu, D. R. Lowy, Isolation of mouse embryo fibroblasts. *Bio. Protoc.* **3**, e908 (2013).
76. R. W. Hunter, M. Foretz, L. Bultot, M. D. Fullerton, M. Deak, F. A. Ross, S. A. Hawley, N. Shpiro, B. Viollet, D. Barron, B. E. Kemp, G. R. Steinberg, D. G. Hardie, K. Sakamoto, Mechanism of action of compound-13: An α1-selective small molecule activator of AMPK. *Chem. Biol.* **21**, 866–879 (2014).
77. T. N. Nguyen, B. S. Padman, J. Usher, V. Oorschot, G. Ramm, M. Lazarou, Atg8 family LC3/GABARAP proteins are crucial for autophagosome-lysosome fusion but not autophagosome formation during PINK1/Parkin mitophagy and starvation. *J. Cell Biol.* **215**, 857–874 (2016).
78. F. Le Guerroué, F. Eck, J. Jung, T. Starzetz, M. Mittelbronn, M. Kaulich, C. Behrends, Autophagosomal content profiling reveals an LC3C-dependent piecemeal mitophagy pathway. *Mol. Cell* **68**, 786–796.e6 (2017).
79. M. Barisic, B. Sohm, P. Mikolcevic, C. Wandke, V. Rauch, T. Ringer, M. Hess, G. Bonn, S. Geley, Spindly/CCDC99 is required for efficient chromosome congression and mitotic checkpoint regulation. *Mol. Biol. Cell* **21**, 1968–1981 (2010).
80. B. Medvar, V. Raghuram, T. Pisitkun, A. Sarkar, M. A. Knepper, Comprehensive database of human E3 ubiquitin ligases: Application to aquaporin-2 regulation. *Physiol. Genomics* **48**, 502–512 (2016).
81. T. Gao, Z. Liu, Y. Wang, H. Cheng, Q. Yang, A. Guo, J. Ren, Y. Xue, UUCD: A family-based database of ubiquitin and ubiquitin-like conjugation. *Nucleic Acids Res.* **41**, D445–D451 (2013).

82. S. P. Kolapalli, R. Sahu, N. R. Chauhan, K. K. Jena, S. Mehto, S. K. Das, A. Jain, M. Rout, R. Dash, R. K. Swain, D. Y. Lee, T. E. Rusten, S. Chauhan, S. Chauhan, RNA-binding RING E3-ligase DZIP3/hRUL138 stabilizes cyclin D1 to drive cell-cycle and cancer progression. *Cancer Res.* **81**, 315–331 (2021).
83. M. Zhang, S. J. Kenny, L. Ge, K. Xu, R. Schekman, Translocation of interleukin-1β into a vesicle intermediate in autophagy-mediated secretion. *eLife* **4**, e11205 (2015).
84. D. Sakellariou, M. Tiberti, T. H. Kleiber, L. Blazquez, A. R. López, M. H. Abildgaard, M. Lubas, J. Bartek, E. Papaleo, L. B. Frankel, eIF4A3 regulates the TFEB-mediated transcriptional response via GSK3B to control autophagy. *Cell Death Differ.* **28**, 3344–3356 (2021).
85. A. R. López, M. H. Jørgensen, J. F. Havelund, F. S. Arendrup, S. P. Kolapalli, T. M. Nielsen, E. Pais, C. J. Beese, A. Abdul-Al, A. C. Vind, J. Bartek, S. Bekker-Jensen, M. Montes, P. Galanos, N. Faergeman, L. Happonen, L. B. Frankel, Autophagy-mediated control of ribosome homeostasis in oncogene-induced senescence. *Cell Rep.* **42**, 113381 (2023).
86. K. Drizyte-Miller, M. B. Schott, M. A. McNiven, Lipid droplet contacts with autophagosomes, lysosomes, and other degradative vesicles. *Contact* **3**, 1–13 (2020).
87. I. Ø. Nielsen, K. Maeda, M. Bilgin, Global monitoring of the mammalian lipidome by quantitative shotgun lipidomics. *Methods Mol. Biol.* **1609**, 123–139 (2017).
88. E. G. Bligh, W. J. Dyer, A rapid method of total lipid extraction and purification. *Can. J. Biochem. Physiol.* **37**, 911–917 (1959).
89. R. Herzog, K. Schuhmann, D. Schwudke, J. L. Sampaio, S. R. Bornstein, M. Schroeder, A. Shevchenko, LipidXplorer: A software for consensual cross-platform lipidomics. *PLOS ONE* **7**, e29851 (2012).
90. R. Herzog, D. Schwudke, K. Schuhmann, J. L. Sampaio, S. R. Bornstein, M. Schroeder, A. Shevchenko, A novel informatics concept for high-throughput shotgun lipidomics based on the molecular fragmentation query language. *Genome Biol.* **12**, R8 (2011).
91. M. Reich, T. Liefeld, J. Gould, J. Lerner, P. Tamayo, J. P. Mesirov, GenePattern 2.0. *Nat. Genet.* **38**, 500–501 (2006).

Acknowledgments: We acknowledge the Core Facility for Integrated Microscopy, Faculty of Health and Medical Sciences, University of Copenhagen for access to the electron microscope. We thank M. Lazarou for providing the HeLa Hexa KO and corresponding control cell lines (*77*). Additionally, we thank the staff at the DCI animal facility, as well as H. Vestergaard, for providing help with animal care, breeding, and experimentation. **Funding:** Work in the Frankel group was supported by the Lundbeck Foundation (R272-2017-3872), the Novo Nordisk Foundation (NNF19OC0057772 and NNF22OC0079880), and the Danish Cancer Society (R352-A20600, R269-A15420, and R209-A13011_001). Work in the Lund group was supported by the Lundbeck Foundation (R218-2016-871 and R233-2016-2819). The Jäättelä group was funded by the Danish National Research Foundation (DNRF125) and the Novo Nordisk Foundation (NNF19OC0054296). K.S. is supported by funding from the Novo Nordisk Foundation (NNF18CC0034900 and NNF23SA0084103). A.J. and T.E.R. were financed by The Norwegian Research Council Toppforsk and Center of Excellence, CanCell grants #262652 and #276070. **Author contributions:** Conceptualization: S.P.K., C.J.B., A.H.L., and L.B.F. Investigation: S.P.K., C.J.B., S.E.R., S.H.B., M.H.J., A.J., M.L., A.A.-A., J.C., A.R.L., J.B.A., K.M., and T.E.R. Methodology: S.P.K., C.J.B., S.E.R., A.H.L., A.J., and K.M. Resources: S.P.K., J.C., A.J., K.S., T.E.R., M.L., J.B.A., and L.B.F. Data curation: S.P.K., C.J.B., S.E.R., M.L., and J.B.A. Validation: S.P.K., C.J.B., M.H.J., A.J., J.B.A., A.R.L., T.E.R., and L.B.F. Software: C.J.B. Formal analysis: S.P.K., C.J.B., S.H.B., S.E.R., J.B.A., A.J., M.L., and L.B.F. Project administration: S.P.K. and L.B.F. Funding acquisition: M.J., A.H.L., K.S., T.E.R., and L.B.F. Visualization: S.P.K., C.J.B., S.E.R., S.H.B., M.H.J., J.B.A., M.L., A.J., and L.B.F. Supervision: M.J., K.S.,T.E.R., A.H.L., and L.B.F. Writing—original draft: S.P.K. and L.B.F. Writing—review and editing: S.P.K., S.E.R., S.H.B., A.R.L., M.J., J.C., K.S., K.M., J.B.A., T.E.R., A.H.L., and L.B.F. All authors agreed to submit the manuscript, read and approved the final draft, and took responsibility for its contents. **Competing interests:** A.H.L. serves as Scientific Advisor to Immagina Biotechnology S.r.l. All other authors declare no competing interests. **Data materials and availability:** All data needed to evaluate the conclusions in the paper are present in the paper and/or the Supplementary Materials. The PELI3 KO mouse can be provided by the Danish Cancer Institute pending scientific review and a completed material transfer agreement. Requests for the PELI3 KO should be submitted to: frankel@cancer.dk.

Submitted 24 June 2024
Accepted 18 December 2024
Published 17 January 2025
10.1126/sciadv.adr2450